Pure appl. geophys. 158 (2001) 1121–1163
0033–4553/01/071121–43 $ 1.50 + 0.20/0

Pure and Applied Geophysics

Tomographic Imaging of *Lg* and *Sn* Propagation in the Middle East

ERIC SANDVOL,[1] KHALED AL-DAMEGH,[1] ALEXANDER CALVERT,[1] DOGAN SEBER,[1] MUAWIA BARAZANGI,[1] RANDA MOHAMAD,[2] RENGIN GÖK,[3] NIYAZI TÜRKELLI[3] and CEMIL GÜRBÜZ[3]

Abstract—Observations based on relatively limited data recorded by sparsely distributed stations have indicated that regional seismic phase propagation (*Lg* and *Sn*) is very complex in the Middle East. Accurate characterization of regional seismic wave propagation in this region necessitates the use of a large number of seismic stations. We have compiled a large data set of regional and local seismograms recorded in the Middle East. This data set comprises approximately four years of data from national short-period networks in Turkey and Syria, data from temporary broadband arrays in Saudi Arabia and the Caspian Sea region, and data from GSN, MEDNET, and GEOFON stations in the Middle East. We have used this data set to decipher the character and pattern of regional seismic wave propagation. We have mapped zones of blockage as well as inefficient and efficient propagation for *Lg*, *Pg*, and *Sn* throughout the Middle East. Two tomographic techniques have been developed in order to objectively determine regions of lithospheric attenuation in the Middle East.

We observe evidence of major increase in *Lg* attenuation, relative to *Pg*, across the Bitlis suture and the Zagros fold and thrust belt, corresponding to the boundary between the Arabian and Eurasian plates. We also observe a zone of inefficient *Sn* propagation along the Dead Sea fault system which coincides with low *Pn* velocities along most of the Dead Sea fault system and with previous observations of poor *Sn* propagation in western Jordan. Our observations indicate that in the northern portion of the Arabian plate (south of the Bitlis suture) there is also a zone of inefficient *Sn* propagation that would not have been predicted from prior measurements of relatively low *Pn* velocities. Mapped high attenuation of *Sn* correlates well with regions of Cenozoic and Holocene basaltic volcanism. These regions of uppermost mantle shear-wave attenuation most probably have anomously hot and possibly thin lithosphere.

Key words: *Lg*, *Sn*, wave propagation, Middle East, tectonics.

[1] Institute for the Study of the Continents, Snee Hall, Cornell University, Ithaca, New York 14853, USA.

[2] Syrian National Seismological Center, General Establishment of Geology and Mineral Resources, Damascus, Syria.

[3] Department of Geophysics, Kandilli Observatory and Earthquake Research Institute, Bogaziçi University, Istanbul, Turkey.

Corresponding Author: e-mail: sandvol@geology.cornell.edu

Introduction

Regional seismograms are dominated by the phases *Pn*, *Pg*, *Sn*, and *Lg*. More often *Sn* and *Lg* are used to infer the attenuation structure of the lithosphere. The seismic phase *Sn* is a high-frequency shear-wave (typically from 1 to 4 Hz and occasionally higher) that travels in the lithospheric mantle above the negative velocity gradient which usually marks the lithosphere-asthenosphere boundary. *Sn* has been reported out to distances of 35° (e.g., MOLNAR and OLIVER, 1969; HUESTIS *et al.*, 1973). *Sn* arrives as a high-frequency wavetrain lasting tens of seconds and up to 1 to 2 minutes. *Sn* velocities are typically 4.7 km/s in stable continental and oceanic lithosphere (HUESTIS *et al.*, 1973) and as low as 4.3 km/s (KADINSKY-CADE *et al.*, 1981) in more tectonically active regions. *Lg* is a complex short period guided wave consisting of high-frequency *P* and *S* energy which travels primarily in the earth's crust at frequencies typically between 0.5 and 5 Hz. It has been modeled as higher-mode Love and Rayleigh waves as well as a sequence of multiply reflected post-critical *S* waves trapped in a crustal guide (BOUCHON, 1982; KENNETT, 1986; BOSTOCK and KENNETT, 1990). *Lg* has been observed not to propagate in oceanic or very thin continental crust (PRESS and EWING, 1952; SEARLE, 1975; ZHANG and LAY, 1995). Both observational and theoretical studies have demonstrated that *Lg* propagation characteristics are primarily a function of the shape of the crustal wave guide (KENNETT, 1986; BOSTOCK and KENNETT, 1990; BAUMGARDT and DER, 1997; RODGERS *et al.*, 1997). There is strong evidence to suggest that rapid changes in crustal thickness will block or weaken *Lg* propagation (BOSTOCK and KENNETT, 1990; FAN and LAY, 1998; MITCHELL *et al.*, 1997). Furthermore, it has been observed that both deep sedimentary basins and intrinsic attenuation can also severely weaken *Lg* propagation (e.g., NUTTLI, 1980; BAUMGARDT and DER, 1997). Recently there have been a number of studies which use *Lg*/*Pg* ratio behavior in terms of crustal waveguide structure (e.g., BAUMGARDT, 1996; FAN and LAY, 1998; HARTSE *et al.*, 1998). This work is critical to isolating path effects from source effects on *Lg*/*Pg* ratios.

Studies of regional wave propagation have yielded important constraints on crustal and uppermost mantle structure and rheology. Studies of *Sn* propagation have helped constrain the rheology of the uppermost mantle in regions such as the Tibetan Plateau where NI and BARAZANGI (1983) and later MCNAMARA *et al.* (1995) documented a region of *Sn* blockage in northern and central Tibet, indicating that this region is probably underlain by thin, hot lithosphere. Similarly, WEIR (1982) found a region in southeastern China where *Sn* was extremely attenuated. Studies of *Lg* propagation have provided valuable insight into crustal structure in the Afar (SEARLE, 1975), Tibet and central Asia (NI and BARAZANGI, 1983; KENNETT, 1986; MITCHELL *et al.*, 1997) and in the Arabian Peninsula (MELLORS *et al.*, 1999).

In the Middle East there are a number of studies of regional wave propagation and its correlation with regional tectonics. Several studies have found that *Lg* coda *Q* values were low (200–500) in tectonically active regions and very low within most of

the Anatolian and Iranian plateaus (MITCHELL *et al.*, 1997; CONG and MITCHELL, 1998). KADINSKY-CADE *et al.* (1982) found a continuous zone of *Sn* attenuation extending from the northern Iranian plateau to central and western Turkey as well as strong evidence of *Lg* blockage across the Zagros fold and thrust belt (Fig. 1a). RODGERS *et al.* (1997) extended this original study using several broadband stations in the region as well as data from the Iranian Long Period Array (ILPA) to extend the regions of *Sn* and *Lg* blockage originally proposed by KADINSKY-CADE *et al.* (1982). RODGERS *et al.* (1997) found a relatively good correlation between regions of inefficient *Sn* propagation and low *Pn* velocities as determined by HEARN and NI (1994). Both MELLORS *et al.* (1999) and RODGERS *et al.* (1997) found evidence for *Sn* attenuation in the Gulf of Aqaba. MELLORS *et al.* (1999) identified evidence for efficient *Lg* propagation across the shield although several other studies had found evidence for low *Lg* coda *Q* in the region (e.g., GHALIB, 1987; SEBER and MITCHELL,

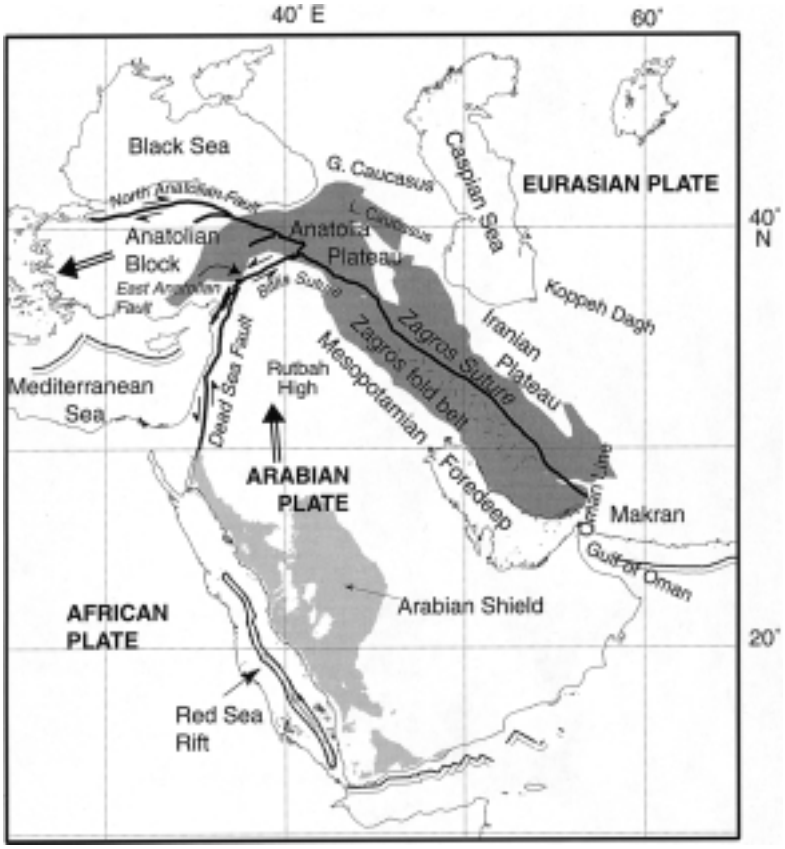

Figure 1a
A simplified tectonic map of the Middle East (after SEBER *et al.*, 1997). Also shown are the major topographic and geographic features. The regions of dark gray correspond to plateau elevations greater than 1500 m. The region of lighter gray corresponds to the Arabian shield.

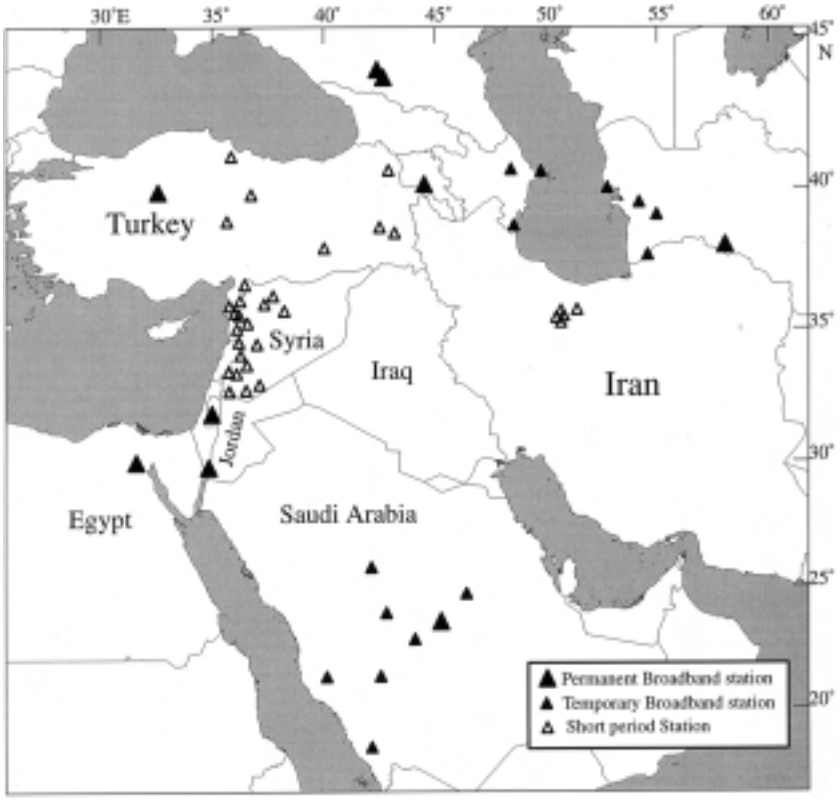

Figure 1b
A map showing all stations and networks used in this study. We have used 65 stations from 6 different networks throughout the Middle East. Open triangles correspond to short-period stations while solid triangles indicate broadband stations. The large solid triangles indicate permanent broadband GSN and GEOFON stations.

1992.). The tomographic model of CONG and MITCHELL (1998) has *Lg* coda *Q* values of approximately 450 in the Arabian shield. All of these studies in the Middle East have utilized a relatively sparse station coverage; this leads to potential ambiguity in the interpretation of *Sn* and *Lg* propagation efficiency since most observations were made using very long paths (~1000 km). Because of the relatively dense station coverage used in this study, we have greatly improved on models of regional wave attenuation in the Middle East.

Tectonic Setting

The Middle East is tectonically and seismically active (Fig. 1a). The major topographic features in the region are the Anatolian–Iranian plateau and Zagros

mountains which formed as a result of the collision between the Arabian plate and Eurasia. This collision is relatively young, having occurred approximately 12 Ma (DEWEY *et al.*, 1986). The Bitlis suture, the Zagros fold and thrust belt, and the East Anatolian left-lateral strike-slip fault mark a distributed, irregular, and young continental collision zone (e.g., SENGOR and KIDD, 1979). Prior to the continental collision, convergence was accommodated by northward subduction of the Neo-Tethys oceanic lithosphere beneath the southern Eurasian margin (DERCOURT *et al.*, 1986). The Anatolian block is escaping to the west (Fig. 1a), as evidenced by the right-lateral strike-slip movement along the North Anatolian fault system (BARKA and REILINGER, 1997) and with left-lateral movement along the East Anatolian fault system (MCKENZIE, 1972, 1976; JACKSON and MCKENZIE, 1988). Within the Anatolian plateau there is extensive Neogene basaltic volcanism with ages younger than 8 Ma (e.g., INNOCENTI *et al.*, 1982; PEARCE *et al.*, 1990) and the majority younger than 3 Ma. Based on their geochemical signature, all of these basaltic volcanics are inferred to be derived from the lower portion of the lithospheric mantle. PEARCE *et al.* (1990) suggests that these basalts were created through heating and localized delamination of the thickened Anatolian lithosphere and subsequent migration of the magma to the surface. PEARCE *et al.* (1990) also suggests a similar type of convective heating of the lithosphere south of the Bitlis suture where similar young basalts are also abundant. Northeast of the Anatolian plateau lies the Lesser and Greater Caucasus which formed, for the most part, synchronously with the collision of the Arabian and Eurasian plates during the middle to late Pliocene (e.g., PHILLIP *et al.*, 1989). Total shortening in the Caucasus has been estimated to be 200 km (DOTDUYEV, 1986). Current shortening rates have been estimated to be approximately 10 mm/yr (REILINGER *et al.*, 1997).

The only active oceanic lithosphere subduction within the Middle East is occurring in the Makran region of southern Iran. The oceanic lithosphere of the Gulf of Oman is being subducted beneath the Eurasian plate. An active volcanic belt associated with this subduction is located approximately 200 km north of the Iranian coast. The Makran is separated from the Zagros collisional belt by the Oman Line (BERBERIAN and KING, 1981; KADINSKY-CADE and BARAZANGI, 1982), which continues northward along the eastern portion of the Lut block in the central Iranian plateau. Northwest of the Makran and west of the Zagros fold and thrust belt is the Mesopotamian foredeep, consisting of thick sediments which increase in thickness eastward (SEBER *et al.*, 1997).

The western edge of the Arabian plate is bounded by the Dead Sea fault in the north and the Red Sea spreading center in the south (Fig. 1a). The Dead Sea fault system, often referred to as the Dead Sea rift, is a leaky transform and has experienced a total slip of about 105 km since the Miocene (e.g., QUENNELL, 1959; FREUND *et al.*, 1970). The majority of this deformation has occurred in the southern portion of the Dead Sea fault system. However, several portions of the fault system are leaky and have produced pull-apart basins such as the Dead Sea trough and the

Gulf of Aqaba (GARFUNKEL, 1981). GARFUNKEL (1981) suggests that spreading centers located in the middle of the pull-apart basins probably extend into the lithospheric mantle and are indicative of considerable lithospheric thinning.

The Arabian shield comprises a series of accreted Proterozoic island arc terranes which were possibly formed during several subduction episodes (GREENWOOD *et al.*, 1980). The northeastern portion of the Arabian shield is the Afif terrane which is composed of granites (640–580 Ma), volcanic rocks, and meta-sediments (660–600 Ma) overlying a crystalline basement (HUSSEINI, 1988). The volcanic fields in particular are very young; 21 eruptions are known to have occurred in the last 1500 years (CAMP *et al.*, 1987). Along the western margin of Saudi Arabia, there is a young active spreading centered along the axis of the Red Sea. To the east the Shield is bounded by the Phanerozoic sedimentary rocks of the Arabian platform which dip gently eastward and overlap the Shield unconformably (POWERS *et al.*, 1966).

Data

In order to understand regional wave propagation behavior in the Middle East we have collected data from local stations in Turkey and Syria, and combined these with broadband stations in the region as well as data from temporary arrays to form a data set of over 5000 seismograms from 65 stations (Fig. 1b) and 2200 events. This large data set has allowed us to achieve resolution in the Middle East that was not available in earlier studies. We used approximately two years of data from 21 short-period stations produced by the newly installed Syrian National Seismic Network (15 vertical component 1 Hz seismometers and six three component instruments); examples of these data are shown in Figure 2. We also used data from short-period single component (vertical) stations in eastern Turkey that are part of the Kandilli Observatory and Earthquake Research Institute network (Fig. 3), these stations are in a region within the Anatolian plateau that previously had no substantial recordings of seismic waveforms. Data from all available permanent three-component broadband stations from the Global Seismographic Network (GSN), Mediterranean Seismographic Network (MEDNET), and German Global Seismographic Network (GEOFON) are also included in our study. Additionally, data collected from single and three-component short-period data from the Iranian Long Period Array (ILPA) as well as data from temporary broadband field deployments in the Caspian Sea and Saudi Arabia were included in our database of seismograms. The ▶

Figure 2

Examples of seismograms produced by the Syrian National Seismic Network. All seismograms are bandpass filtered with corner frequencies at 1 and 4 Hz. These seismograms demonstrate the inefficient *Sn* propagation in the western Arabian plate as opposed to the efficient *Sn* propagation we observe in the Mediterranean. All three of the recordings are taken from single component short-period seismometers. The gray lines are faults, the solid triangles are seismic stations, and the solid circles are earthquakes.

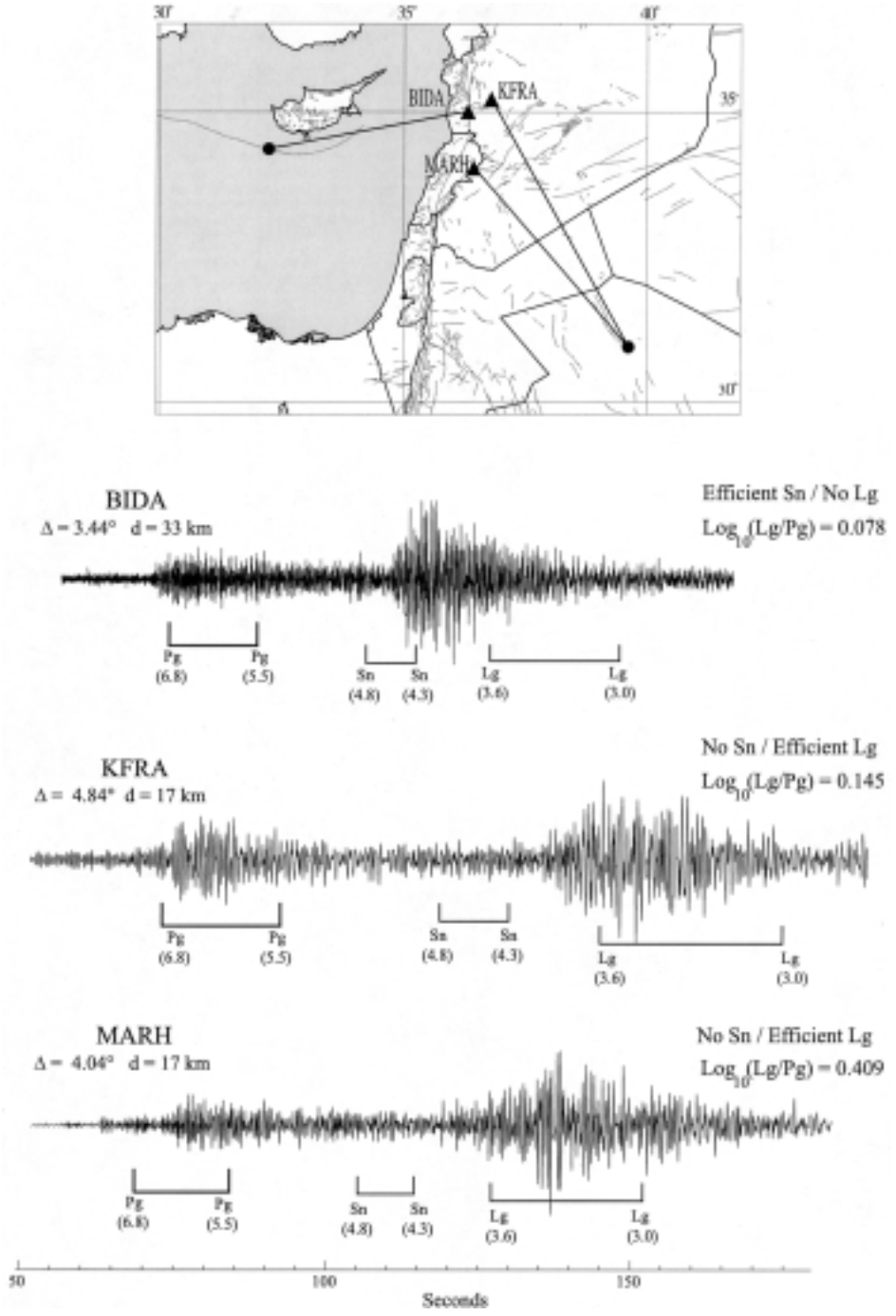
30°
35°
40°
35°
30°
BIDA
KFRA
MARH
BIDA
Δ = 3.44° d = 33 km
Efficient Sn / No Lg
Log10(Lg/Pg) = 0.078
KFRA
Δ = 4.84° d = 17 km
No Sn / Efficient Lg
Log10(Lg/Pg) = 0.145
MARH
Δ = 4.04° d = 17 km
No Sn / Efficient Lg
Log10(Lg/Pg) = 0.409
Pg (6.8)
Pg (5.5)
Sn (4.8)
Sn (4.3)
Lg (3.6)
Lg (3.0)
50
100
150
Seconds

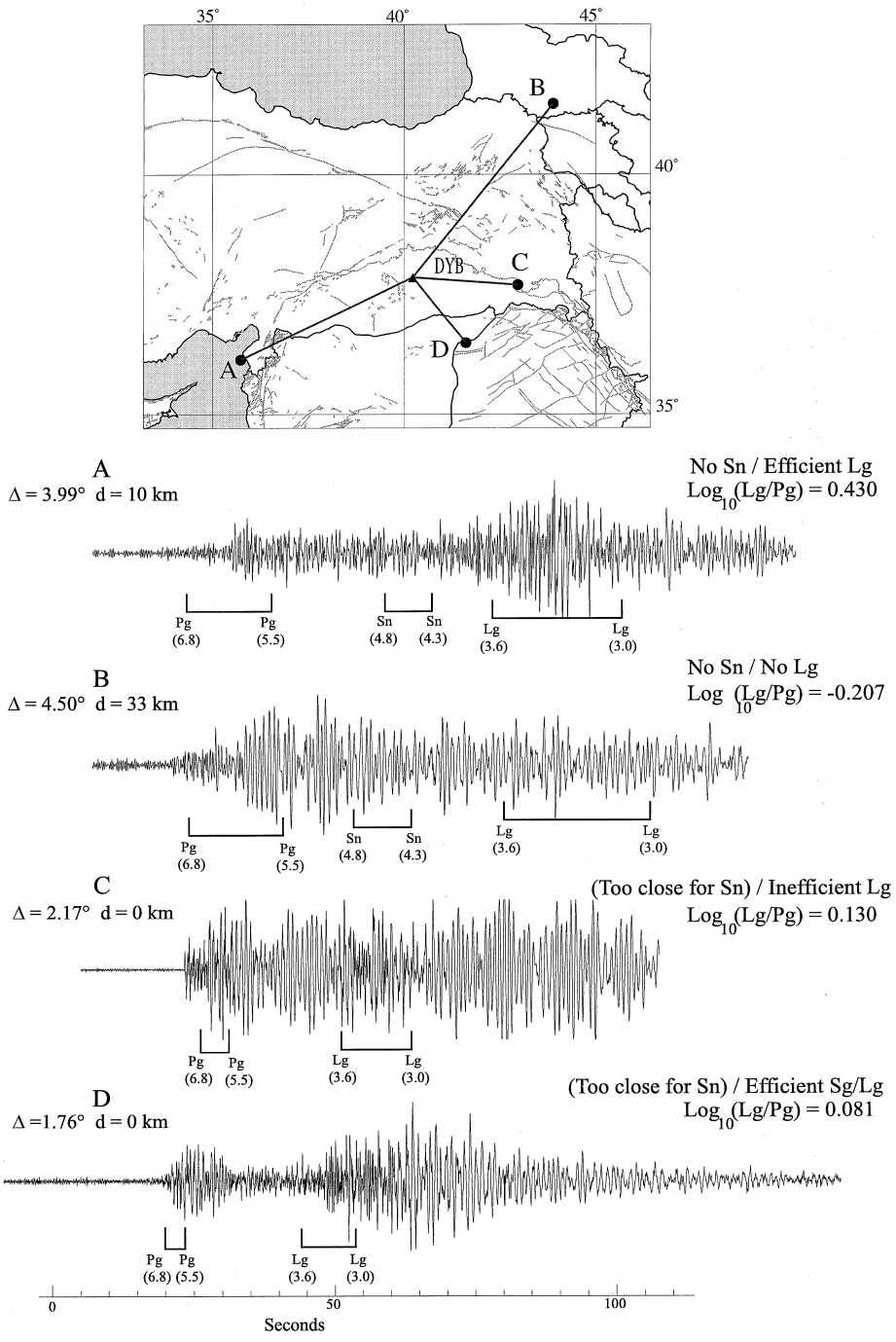
35°
40°
45°
40°
35°
A
B
C
D
DYB
A
Δ = 3.99° d = 10 km
No Sn / Efficient Lg
Log10(Lg/Pg) = 0.430
Pg (6.8)
Pg (5.5)
Sn (4.8)
Sn (4.3)
Lg (3.6)
Lg (3.0)
B
Δ = 4.50° d = 33 km
No Sn / No Lg
Log10(Lg/Pg) = -0.207
C
Δ = 2.17° d = 0 km
(Too close for Sn) / Inefficient Lg
Log10(Lg/Pg) = 0.130
D
Δ =1.76° d = 0 km
(Too close for Sn) / Efficient Sg/Lg
Log10(Lg/Pg) = 0.081
0
50
100
Seconds

Saudi Arabian broadband experiment recorded extremely high-quality broadband regional seismograms starting in November 1995 and terminating in January 1997 (Fig. 4); we collected over 1200 seismograms from this experiment alone. The Caspian Sea Experiment included eight three-component broadband stations both to the east and west of the Caspian Sea (MANGINO and PRIESTLEY, 1998) and recorded approximately eighty seismic events well enough to be included in our study (Fig. 5).

All 5000 seismograms in our regional waveform database have been reviewed by applying a range of bandpass filters in order to identify the relevant regional phases. Those seismograms that were saturated, had low signal-to-noise, or included large amounts of electronic noise were not included in our database. Seismograms with sampling rates of less than 10 sps were also discarded. Distances between 175 km to 2000 km were used for our *Lg* observations and a variety of bandpass filters were applied to test the frequency dependence of this phase. We discarded any *Lg* seismograms for events with hypocentral depths larger than 40 km. In order to identify *Sn* we applied bandpass filters between 1 to 4 Hz and 2 to 5 Hz. For *Sn* we included all seismograms between 330 and 2000 km. We avoided potential confusion with direct *S* arrival by applying filters in travel-time windows that should only include *Sn* rather than *S* at distances past 1500 km. We did identify direct *S*-wave arrivals for many regional seismograms but noticed a distinct difference in the waveform shape and frequency content; therefore, we were able to distinguish between the different arrivals.

Lg Propagation in the Middle East

Lg/*Pg* ratios are generally used in discriminating earthquakes from explosions. In order to determine the path effects on *Lg*/*Pg* amplitude ratios and to characterize *Lg* propagation (relative to *Pg*) we have computed approximately 4400 *Lg*/*Pg* amplitude ratios. We have tomographically mapped the variations in *Lg*/*Pg* ratios throughout the Middle East. For this study, we defined *Lg* as the energy within a group velocity window of 3.0 km/s to 3.6 km/s. For *Pg* we used a group velocity window of 5.5 to 6.8 km/s. We calculated the group velocity window for *Lg* and *Pg* group velocity window relative to the first arrival for all seismograms. This technique has the advantage of eliminating errors caused by network timing errors as well as minimizing effects from possible source mislocations. The amplitude ratios were

◀

Figure 3

Examples of vertical component seismograms recorded by station DYB. All seismograms shown are bandpass filtered with corner frequencies at 1 and 4 Hz. These seismograms show the difference in *Lg* propagation in the Anatolian plateau and in the northern Arabian plate. For events A and B we do not observe any *Sn* signal on any of the three components seismograms. The gray lines are faults, the solid triangles are seismic stations, and the solid circles are earthquakes.

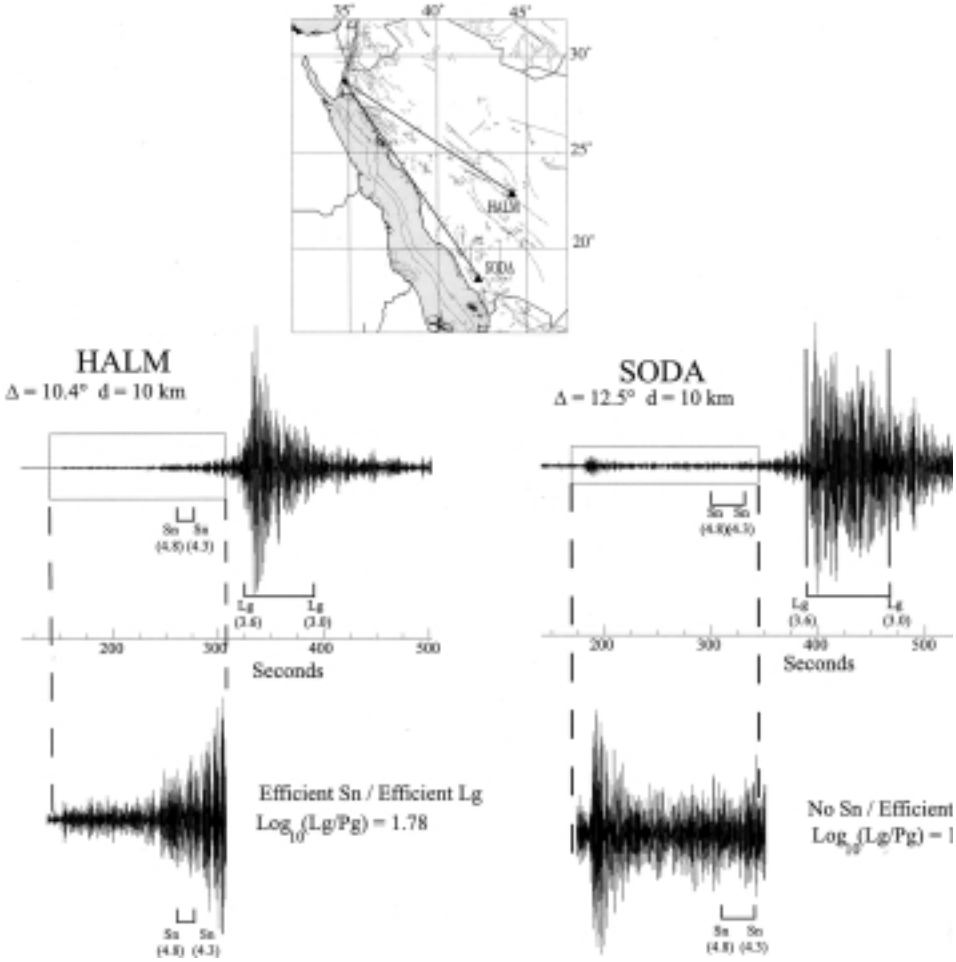

Figure 4
Two examples of vertical broadband seismograms taken from temporary stations in the Arabian shield. The seismograms were filtered with a bandpass filter with corner frequencies at 1 and 4 Hz. These records clearly indicate that *Lg* is an efficient phase across this portion of the Arabian shield. Furthermore, a very clear difference in *Sn* efficiency can be seen for the Red Sea coastal path (station SODA) and the interior Arabian shield path. The gray lines are faults, the solid triangles are seismic stations, and the solid circles are earthquakes.

calculated by taking the logarithm of the ratio of the root-mean-square (RMS) of the amplitudes in the group velocity window in the time domain (*Lg* and *Pg*):

$$D = \mathrm{Log}_{10}\{\mathrm{RMS}\ [Lg]/\mathrm{RMS}\ [Pg]\}\ . \qquad (1)$$

Maximum absolute amplitude ratios were also used although we found them to be less stable than the RMS amplitude ratios. We tested the sensitivity of our *Lg*/*Pg*

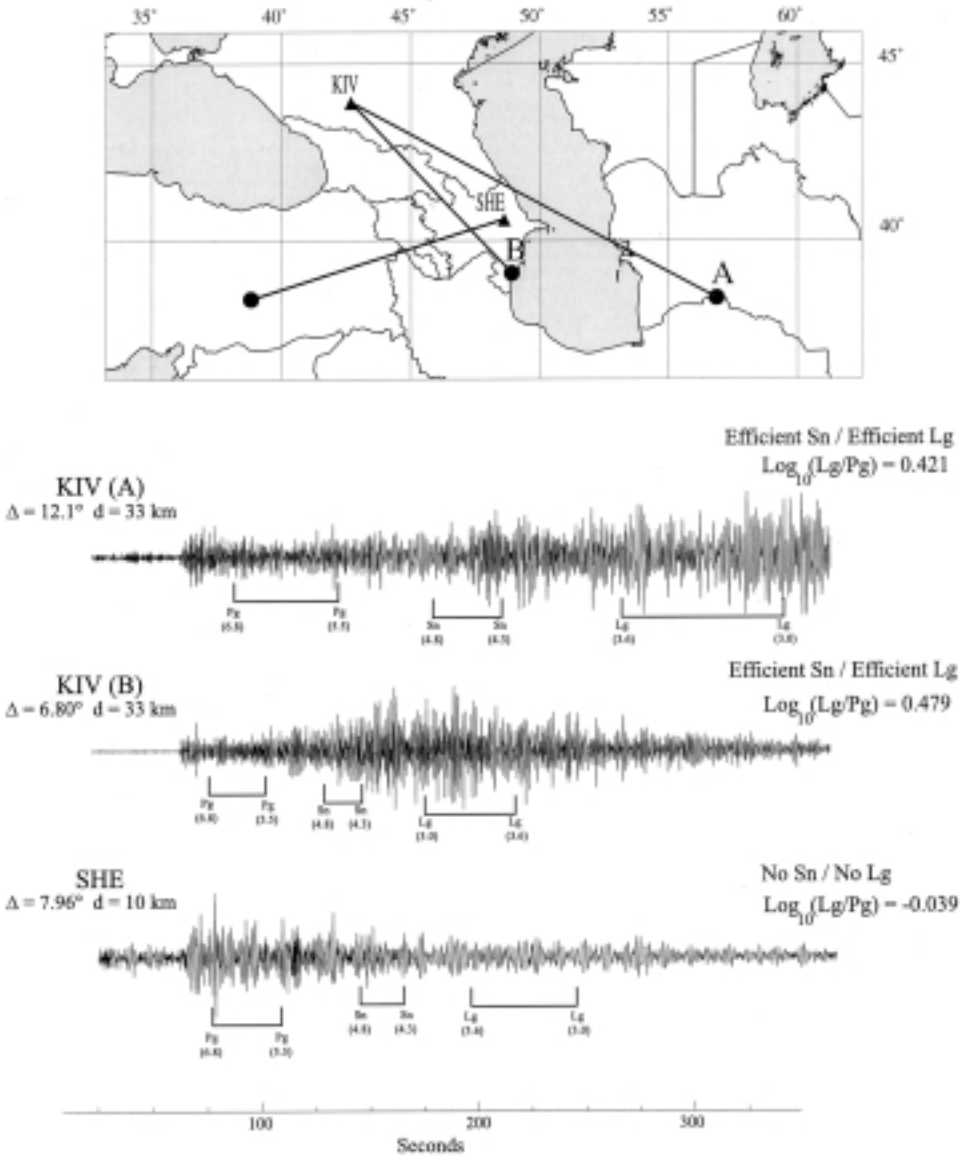

Figure 5

Examples of seismograms taken from the Caspian Sea region. Stations SHE and KIV are three component broadband stations that were a part of the temporary deployment of stations between 1993 and 1996 (MANGINO and PRIESTLEY, 1998). Station KIV is a broadband station which is part of the Global Seismographic Network (GSN). These records clearly indicate the difference in wave propagation across the north Caspian Sea and the southern Caspian Sea, as well as the *Lg* blockage in the easternmost Anatolian plateau. These seismograms also demonstrate the difference in *Sn* propagation across the Caspian Sea (station KIV) as opposed to the paths that cross the Anatolian plateau (station SHE). All seismograms are bandpassed filtered (1–4 Hz). The solid triangles are seismic stations, and the solid circles are earthquakes.

ratios to the *Lg* group velocity window and found that if we vary the group velocity windows by 0.2 km/s the calculated RMS *Lg*/*Pg* ratios did not vary by more than 10 percent.

In order to further verify that the calculated *Lg*/*Pg* ratios are representative of our seismic waveforms, we visually inspected all of the waveforms in our study. Each event-station pair was assigned an efficiency that corresponded to either efficient *Lg*, inefficient *Lg*, or absent or blocked *Lg*. We found a fairly high degree of correlation between our visual inspections and the *Lg*/*Pg* ratios. Generally the *Lg*/*Pg* ratios close to one (Fig. 6) corresponded to weak or inefficient *Lg* propagation while *Lg*/*Pg* ratios of less than one corresponded to blocked *Lg* (Fig. 7). Seismograms with very efficient *Lg* phases usually had *Lg*/*Pg* ratios larger than 5.0 although some seismograms did have anomously high *Pg* amplitudes for paths crossing large sedimentary basins, which decreased the amplitude of the *Lg*/*Pg* ratios significantly.

Method

We have applied tomographic techniques to make more objective and quantitative measurements of the propagation efficiencies in the Middle East. Also, we have a very large data set (>4400 raypaths) in which mapping by visual inspection is difficult (Fig. 8). In order to tomographically map the regional variation of our *Lg*/*Pg* ratios we derived a linear relationship between amplitude ratios and path length. Following the derivation of PHILLIPS *et al.* (1999) and the starting model of CONG *et al.* (1996), we assume that seismic phase amplitudes (a_{ijk}) can be modeled using the following relation for a given frequency band:

$$a_{ijk}(\omega) = L_{ij}^{-\beta_k} s_{jk}(\omega) c_{ik}(\omega) \exp[\alpha_k(\omega) L_{ij}] \ , \tag{2}$$

where β_k is the geometrical spreading exponent for the k-th phase, s_{jk} is the station response for the j-th station and for the k-th phase, c_{ik} is the source scaling term for the i-th seismic source and the k-th phase, L_{ij} is the total raypath length, and α_k is the spatial average attenuation coefficient and is assumed to be constant over a given frequency band. If we take the logarithm of the amplitude ratio of two phases (1 and 2) and then discretize the spatial attenuation factor:

$$\Delta A_{ij} = \Delta S_j + \Delta C_i + \Delta\beta \log_{10} L_{ij} + \log_{10} e \sum_l \Delta m_l l_{ijl} \ , \tag{3}$$

▶

Figure 6

Examples of waveforms recorded by a variety of stations in the Anatolian plateau and the northern Arabian plate. Station ANTO is a three-component broadband GSN station while BNN and DYB are short-period single component stations. Stations QASN and SLMH are also single component short period. All of these data show waveform shapes typical of regional paths crossing the Anatolian plateau (weak *Lg* and little or no *Sn*). All seismograms are bandpassed filtered (1–4 Hz). The gray lines are faults, the solid triangles are seismic stations, and the solid circles are earthquakes.

where

$$\Delta A_{ij} = \log_{10}(a_{ij1}/a_{ij2}), \quad \Delta C_i = \log_{10} c_{i1} - \log_{10} c_{i2} \ ,$$
$$\Delta S_j = \log_{10} s_{j1} - \log_{10} s_{j2}, \quad \text{and} \quad \Delta m = \alpha_2 - \alpha_1 \ .$$

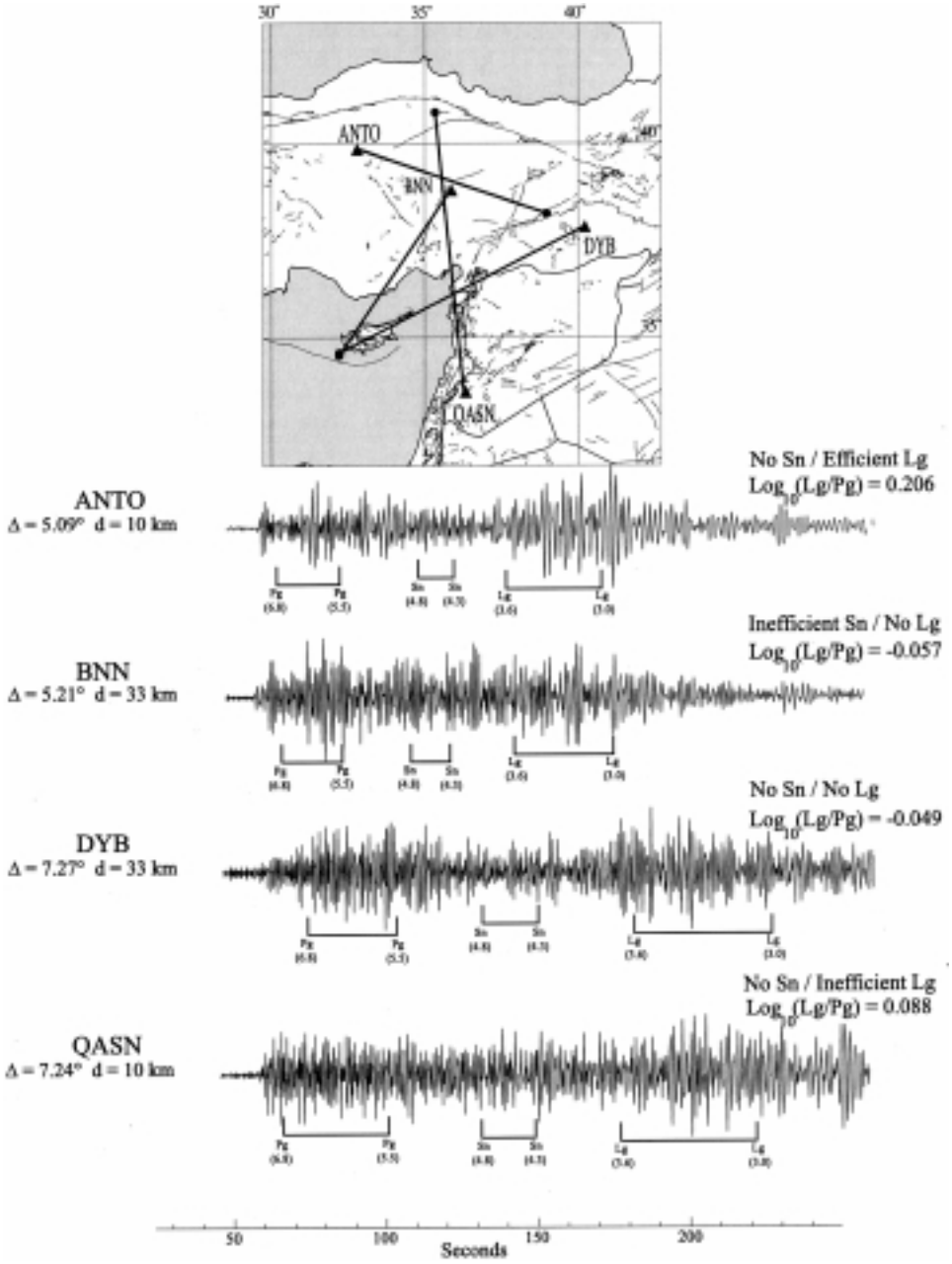

ΔA_{ij} is the logarithm of the phase amplitude ratio, ΔS_j is the logarithm ratio in instrument response for each phase, ΔC_i is the differential source scaling term, $\Delta\beta$ is the differential geometric spreading factor between each phase, Δm_{il} are the model spatial attenuation factors for the l-th cell and i-th ray, and l_{ijl} the length of the ray in the l-th cell. If we assume $s_{j1} = s_{j2}$ and a linear and constant relationship independent of frequency between Pg and Lg source scaling (i.e., $\Delta C_i = \Delta C$):

$$\Delta A_{ij} = \Delta C + \Delta\beta \log_{10} L_{ij} + \log_{10} e \sum_l \Delta m_l l_{ijl} \quad . \tag{4}$$

We would expect ΔS_j to be zero as long as the seismometer response is flat for all stations over the frequency band of interest. In order to linearize this system of equations we expand equation (4) to obtain:

$$\Delta A_{ij} = \Delta C + \Delta\beta \log_{10} L_{ij} + \log_{10} e\, \Delta\mathbf{M} L_{ij} + \log_{10} e \sum_l m_l l_{ijl} \tag{5}$$

where $\Delta\mathbf{M}$ is the mean spatial attenuation parameter and Δm_l are the mean corrected spatial attenutaion parameters. We can then solve for ΔC, $\Delta\beta$, and $\Delta\mathbf{M}$ and subtract this portion of equation (5) from ΔA_{ij}:

$$\Delta \acute{A}_{ij} = \log_{10} e \sum_l \Delta m_l l_{ijl} \tag{6}$$

where

$$\Delta \acute{A}_{ij} = \Delta A_{ij} - \Delta C - \Delta\beta \log_{10} L_{ij} - \log_{10} e\, \Delta\mathbf{M} L_{ij} \quad .$$

In practice we found that including $\log_{10} e\, \Delta\mathbf{M}$ made little difference for our data set. Equation (6) is a linear set of equations which relates the spatial change in the difference in Lg and Pg attenuation to our corrected Lg/Pg amplitude ratios.

In order to solve the linear system of equations we used the LSQR method of PAIGE and SAUNDERS (1982). This method has the advantage of not introducing any hidden scaling into the solution as well as providing an objective regularization scheme (NOLET, 1988). We spatially regularized our results using Laplacian damping which has been used successfully elsewhere to minimize inversion artifacts (e.g., MEYERS *et al.*, 1998). We tested a variety of Laplacian damping weights and selected one which minimizes tomographic artifacts while maintaining our spatial resolution.

▶

Figure 7

Four seismograms demonstrating the strong *Sn* attenuation occurring between eastern Jordan to northwestern Saudi Arabia. Stations (BDRN and SALA) in western Syria record a very clear *Sn* while stations in the Arabian shield (UQSK and TAIF) record no *Sn*. All seismograms are bandpassed filtered (1–4 Hz). The solid triangles are seismic stations and the solid circles are earthquakes. Note the *Sn* to *Lg* converted phases with group velocities of 3.5 to 4.0 km/s for station UQSK and TAIF.

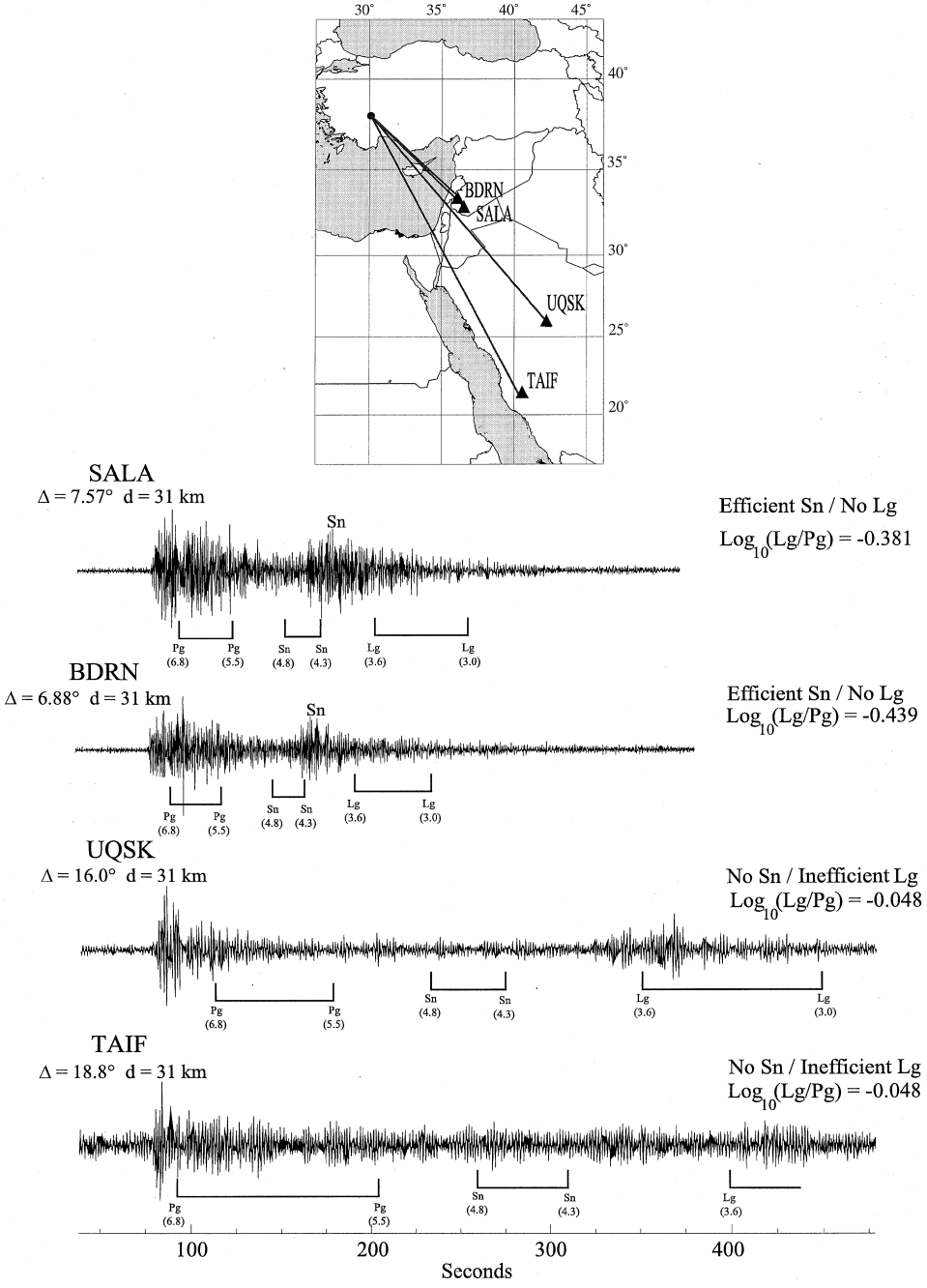
30°
35°
40°
45°
40°
35°
30°
25°
20°
BDRN
SALA
UQSK
TAIF
SALA
Δ = 7.57° d = 31 km
Sn
Pg (6.8)
Pg (5.5)
Sn (4.8)
Sn (4.3)
Lg (3.6)
Lg (3.0)
Efficient Sn / No Lg
Log10(Lg/Pg) = -0.381
BDRN
Δ = 6.88° d = 31 km
Efficient Sn / No Lg
Log10(Lg/Pg) = -0.439
UQSK
Δ = 16.0° d = 31 km
No Sn / Inefficient Lg
Log10(Lg/Pg) = -0.048
TAIF
Δ = 18.8° d = 31 km
No Sn / Inefficient Lg
Log10(Lg/Pg) = -0.048
100
200
300
400
Seconds

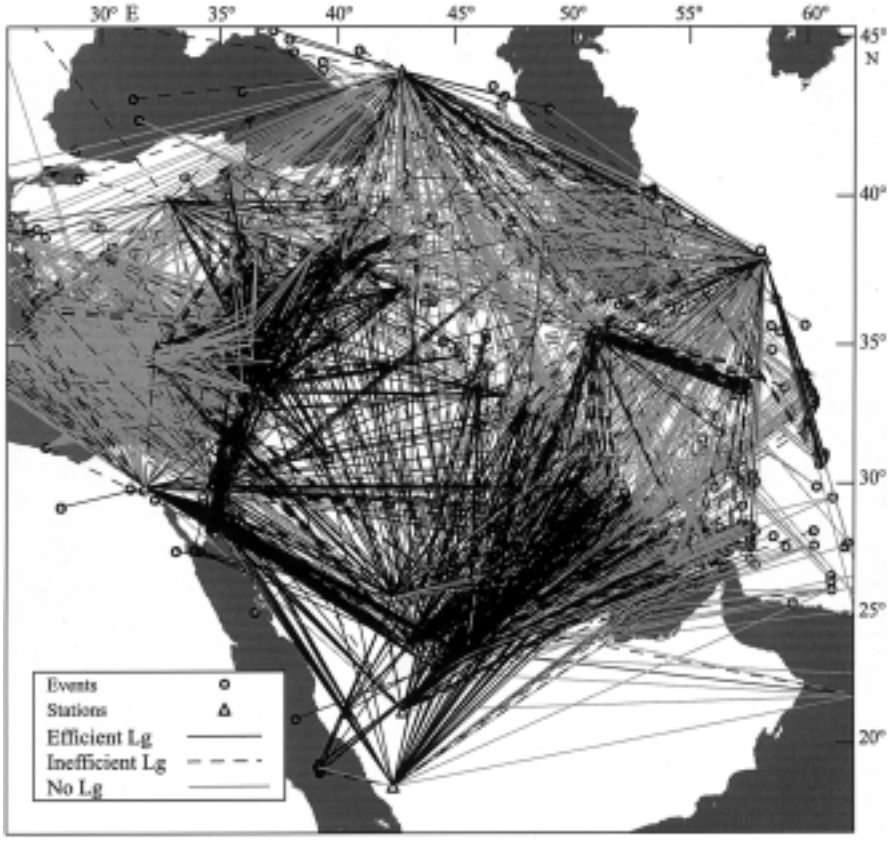

Figure 8
A map showing raypaths for all 4400 event-station pairs used in our *Lg* analysis. The efficiencies shown (efficient, inefficient, blocked) are taken from our visual inspection of each seismogram. Approximately 4200 raypaths are shown. *Lg* attenuation caused by the Iranian plateau, Mediterranean, Caspian and Black Sea can be clearly seen.

We have tested for bias or errors caused by the various instrument and station types by including the ΔS_j term in our inversion (equation (3)). We found that this term did not significantly affect our results although we did observe, for those isolated stations, some path-station corrections trade-off. We found that the attenuation structure near those stations tended to be more "damped" and of smaller amplitude than when the station corrections were not included.

Owing to the difference in geometrical spreading between *Pg* and *Lg*, many studies have shown a strong *Lg*/*Pg* ratio distance dependence (e.g., FAN and LAY, 1998). We have included this in our inversion ($\Delta\beta$) by solving the linear *Lg*/*Pg* ratio dependence on the logarithm of the path length. We found only a weak distance dependence in the Middle East, primarily because of substantial blockage and

attenuation that both *Lg* and *Pg* undergo in the Middle East (Fig. 9). The resulting model of spatial attenuation is representative of our observed spatial variation in the *Lg*/*Pg* amplitude ratios in the Middle East neglecting possible source effects (Fig. 10). The amplitude of *Pg*, in particular, could potentially vary with respect to the source mechanism; however, any potential bias in our tomographic model should be lessened by redundant raypaths.

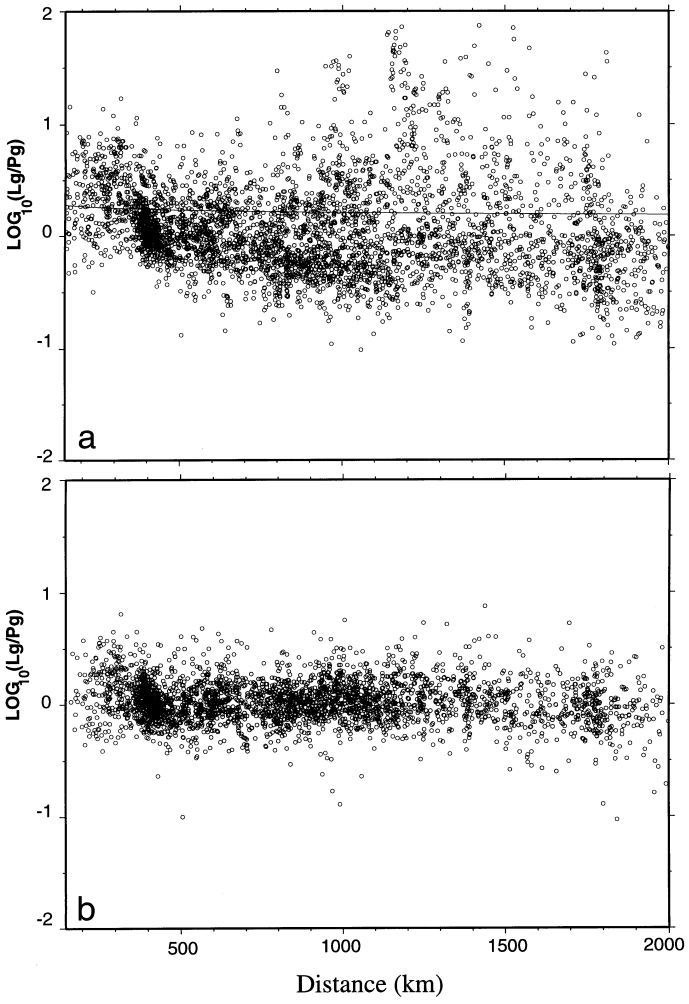

Figure 9
Plots showing all *Lg*/*Pg* amplitude ratios (versus distance) calculated for each ray-path shown in Figure 8. The line in panel (a), is the best fit for the logarithm of the distance. Panel (b) shows the residuals after 12 iterations using a Laplacian damped LSQR algorithm. There was a 50 percent reduction in the variance of the *Lg*/*Pg* ratios using our tomographic model. 95% of all *Lg*/*Pg* ratios fell within ± 0.4.

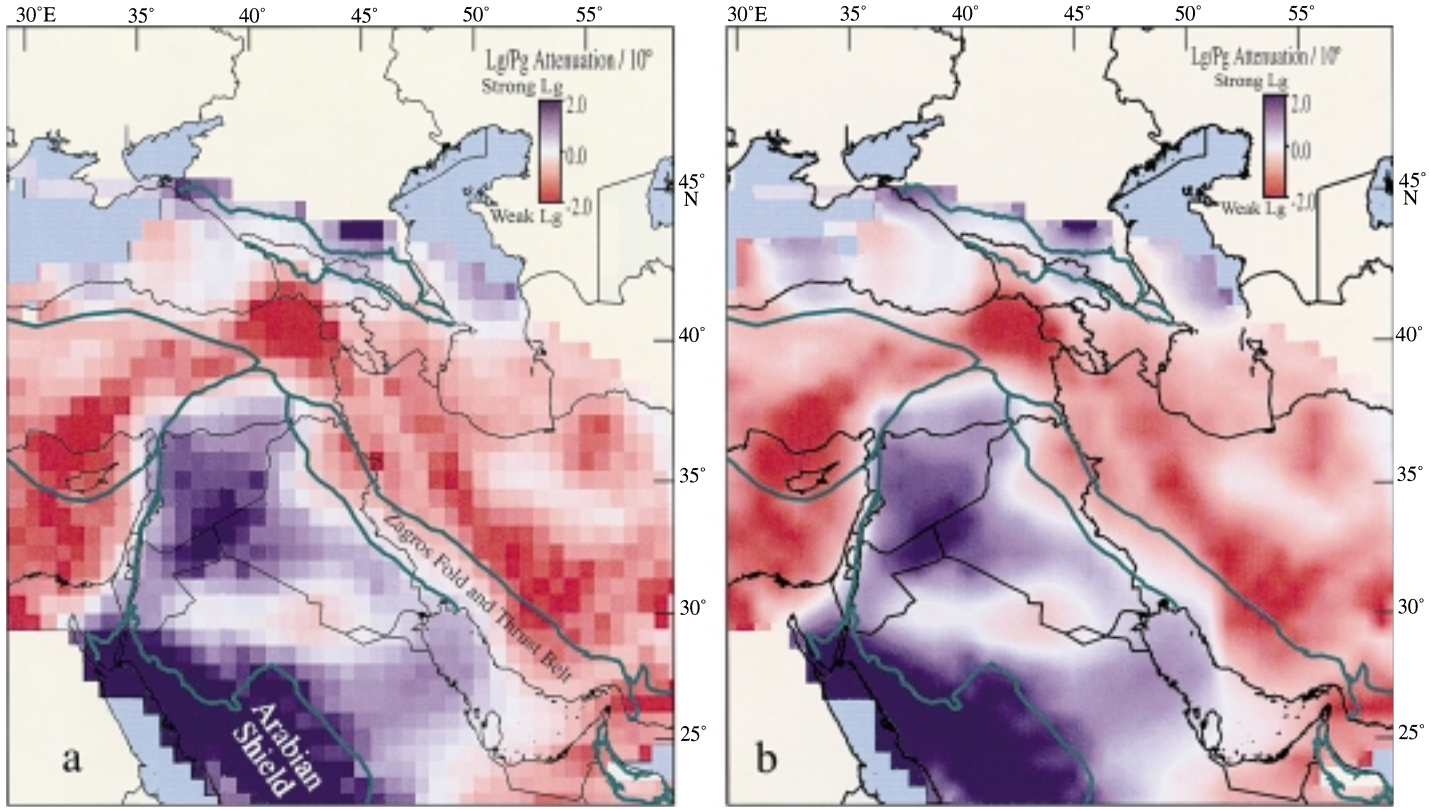

Figure 10
Maps showing *Lg*/*Pg* tomographic model for frequencies between 1 and 4 Hz. The clearest feature is the generally efficient *Lg* propagation within the Arabian plate and the weak or blocked *Lg* propagation within the Anatolian and Iranian plateaus. Panel (a) shows the raw tomographic model while panel (b) is the linearly interpolated model. In panel (a) and (b) the green lines show the major tectonic boundaries in the Middle East.

Resolution and Uncertainty

In order to test the resolution and stability of our tomographic model we performed several resolution and error tests. We would expect to obtain the highest resolution and most reliable solutions in regions of dense ray coverage. Generally we have good ray coverage, except at the model edges, throughout most of our model (Fig. 11). However, due to lack of stations and sources in Iraq and eastern Jordan we have limited resolution and a less reliable attenuation model for this subregion.

A standard test applied in most tomographic studies is to test model resolution using synthetic checkerboards or spikes to generate a synthetic data set with the same raypaths as the actual data set. We have also added Gaussian noise to the synthetic data set with amplitudes equal to $\pm 15\%$ of the maximum synthetic Lg/Pg ratio. This synthetic data set is then inverted and compared to the original synthetic input model. We employed this technique using a variety of synthetic model geometries

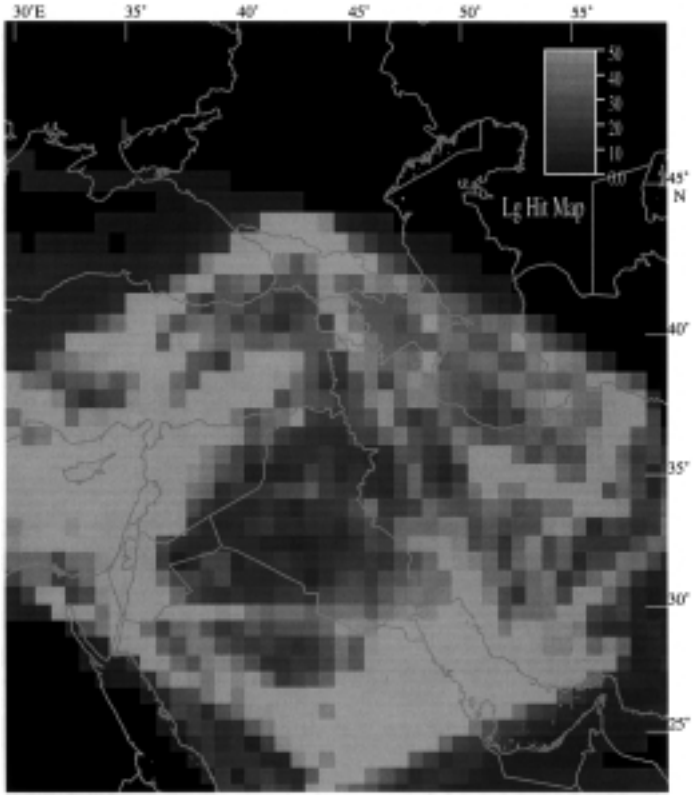

Figure 11
A map showing the hit counts for each cell in the tomographic model shown in Figure 10. Note the smaller hit counts in western and central Iraq. This is a region where the resolution is the poorest and the uncertainties are the largest.

ranging from checkerboards to vertical and horizontal stripes, as well as spike tests. The results of one spike test are shown in Figure 12. We used the same Laplacian damping weights and number of inversion iterations as were used with our original tomographic inversion. Considerable ''smearing'' can be seen, especially in those regions with limited ray coverage. In particular, dramatic distortion of the synthetic anomalies in Saudi Arabia is occurring due to the multitude of raypaths which travel across the Mediterranean into Saudi Arabia (Fig. 12b). Since there is very limited station coverage in this region and even fewer earthquakes, it is not surprising to see this type of artifact. The Gulf region also has relatively poor resolution. However, we have fairly good resolution in Anatolia, the eastern Mediterranean, and Syria.

We also tested the stability of our tomographic model by using a bootstrap resampling technique. This test should detect any regions of the model which are

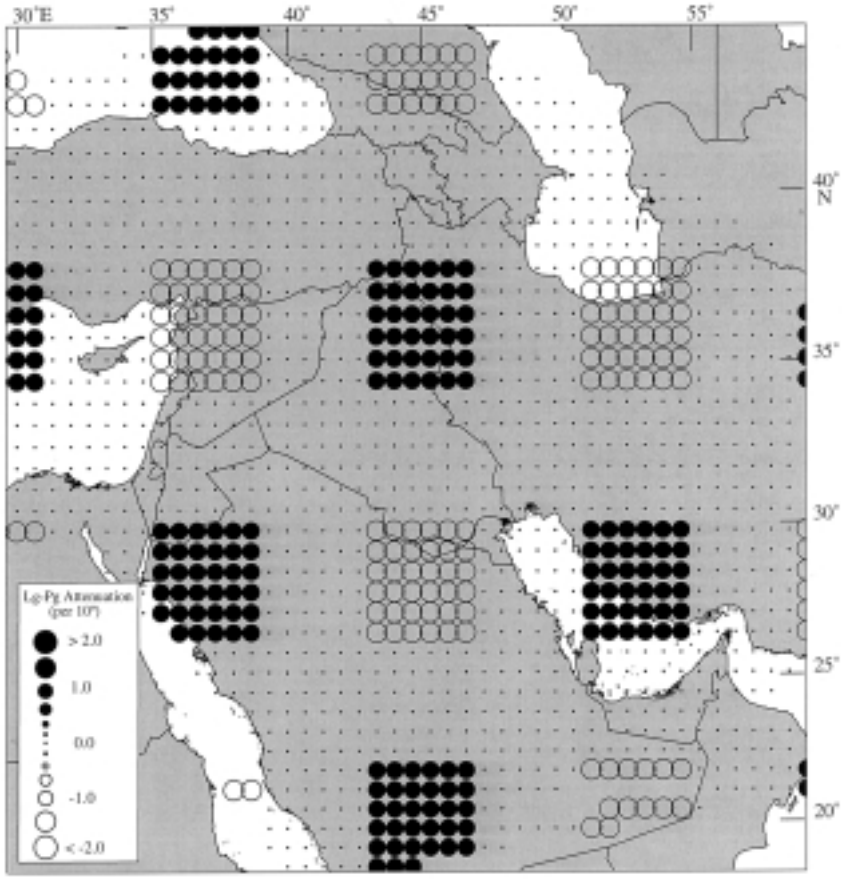

Figure 12a
A map showing one of the test models we have used for determining the resolution of our *Lg-Pg* differential attenuation model. This model contains spikes with alternating positive and negative anomalies of 2×10^{-3}.

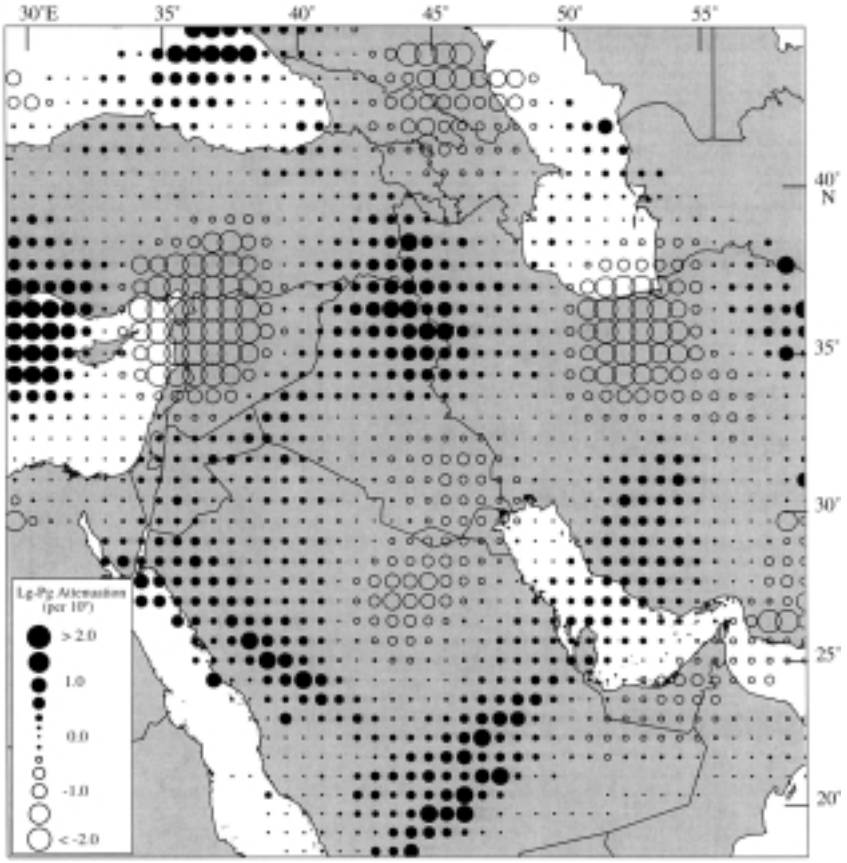

Figure 12b
A map showing the results of our resolution test for the starting model shown in Figure 12a. Note the abundant smearing that occurs in the Arabian/Persian Gulf and in northwestern Saudi Arabia. These are regions where our resolution is the poorest.

dependent on only a few inconsistent observations (HEARN and NI, 1994). We randomly resampled our raypaths until we reached the same number of observations as in our original inversion. This resampled data set is then inverted; this procedure is repeated 100 times, giving us a distribution from which a variance can be calculated. We found that the bootstrap variances converged after approximately 100 bootstrap iterations. These variances are shown in Figure 13. For our *Lg*/*Pg* model we generally have very small uncertainties; only those cells on the edge of the model (e.g., in the Red Sea and easternmost Egypt) exceed variances of more than 0.1. These results also suggest that our data set is not overly sensitive to source focal mechanisms since variations in *Lg*/*Pg* amplitude ratios due to source type should be apparent in our bootstrap uncertainty estimates as long as the distribution of source focal mechanisms is not entirely systematic.

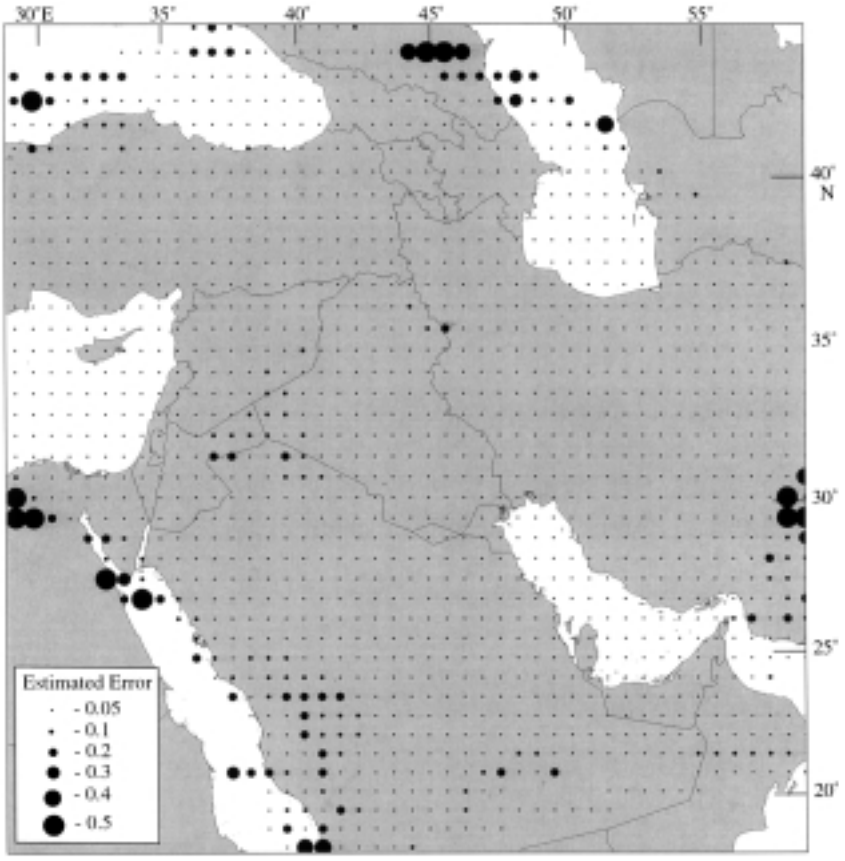

Figure 13
A map showing the bootstrap uncertainty estimates for the *Lg*/*Pg* tomographic model shown in Figure 10. These uncertainty estimates were calculated after 100 bootstrap iterations. Generally our solution was very stable. Only on the edge of our model do we find uncertainties significantly larger than 0.10.

Results

The most striking result of our *Lg*/*Pg* tomography is that regions of small *Lg*/*Pg* ratios mainly correspond with continental collision zones in the Middle East (Figs. 1 and 10). The regions near the Bitlis suture and the Zagros fold and thrust belt are both delineated very clearly in our model as zones of *Lg* blockage. Within both the Iranian and Anatolian plateaus, *Lg* propagation with respect to *Pg* is generally inefficient or weak. We do observe some inefficient *Lg* phases within the central Iranian plateau. Within the entire Anatolian plateau, however, *Lg* is inefficient. In the Lesser Caucasus and the extreme western part of the greater Caucasus there is a large region where *Lg* is either blocked or inefficient (Figs. 5 and 10). Within the

south Caspian Sea basin *Lg* is also blocked; however, the northern Caspian Sea appears to have fairly efficient *Lg* propagation.

We also observe large regions of very efficient *Lg* propagation. Within the Arabian shield we observe very efficient *Lg* propagation (Figs. 4 and 10) which is consistent with the observations of MELLORS *et al.* (1999) and with the *Lg* coda *Q* models of CONG and MITCHELL (1998). Our tomographic image very clearly outlines the Arabian shield where we have very large (~2.0) *Lg-Pg* differential spatial attenuation while we have more modest differential attenuation (~0.5) in the Arabian platform and Mesopotamian foredeep. Another large region of very efficient *Lg* propagation is an area in western Iraq and eastern Jordan. This anomaly, however, is somewhat suspect since this is a region of relatively poor ray coverage (Fig. 13). We also found that the *Lg* to *Sn* converted phases, such as those shown in Figure 7, did not have a major impact upon our tomographic model. This is due primarily to the small amplitudes of such converted phases as well as the numerous stations and events that we have used in our inversion.

Another important issue regarding *Lg* propagation is the frequency dependence of the *Lg*/*Pg* ratios. Different crustal structure and rheologies can have different responses to different seismic frequencies. In order to investigate the frequency dependence of *Lg*/*Pg* ratios in the Middle East we applied a number of narrow bandpass filters to our seismogram database and tomographically mapped the resulting *Lg-Pg* differential attenuation. Figure 14a shows the same image shown in Figure 10 for reference. This image corresponds to a frequency band of 1 to 4 Hz. Figures 14b and 14c show progressively higher frequency bands. In general there is no appreciable change in the models until the frequency band of 2 to 4 Hz. Many of the larger model attenuation anomalies, seen in Figures 14a, 14b, and 14c, have been reduced considerably. There is also more *Lg* attenuation and less *Pg* attenuation in the Mesopotamian foredeep and less in the Lesser Caucasus than in the other lower frequency models.

We obtained a 50 percent variation reduction in our ratio residuals (Fig. 9) for the frequency band between 1 and 4 Hz. We obtained similar variance reductions for the other frequency bands that we analyzed, except for the 2–4 Hz band which had a variance reduction of 48 percent. This smaller variance reduction is due to the poor data quality (low signal-to-noise ratio) for this frequency band. After applying path corrections obtained from our model, the resulting 95% of our corrected residual fell within ± 0.4 of zero (Fig. 9), indicating that we have successfully removed a large portion of the path effects for *Lg*/*Pg* ratios in the Middle East.

Sn Propagation in the Middle East

In order to map *Sn* attenuation in the Middle East we reviewed and determined the *Sn* propagation efficiencies into three categories for over 4200 seismograms. The

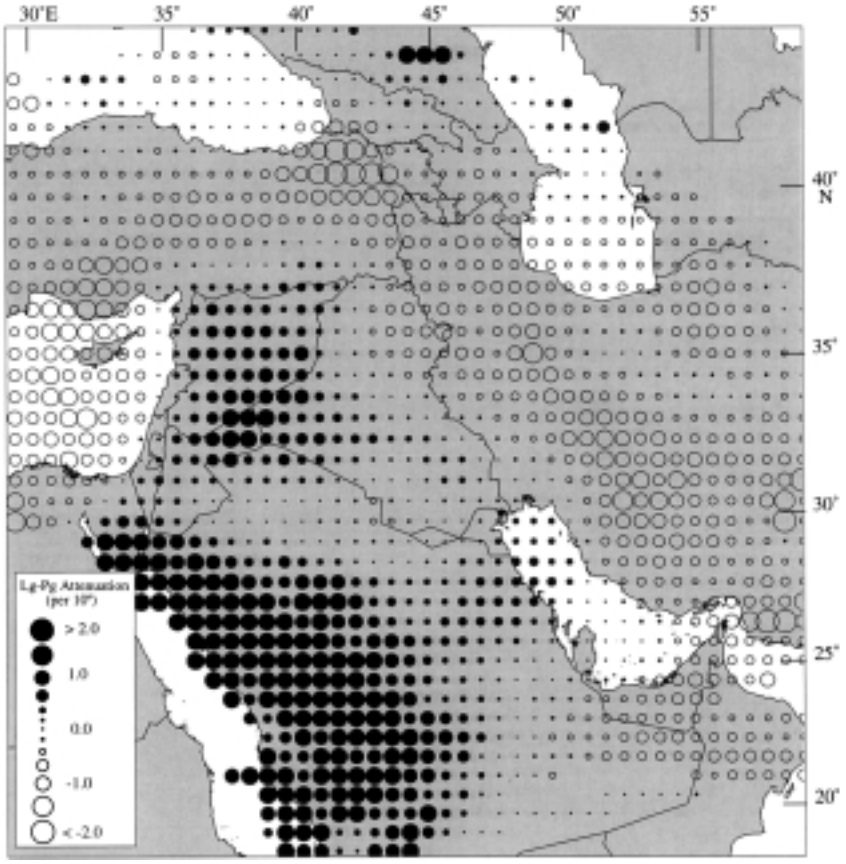

Figure 14a
A map showing a tomographic model of *Lg*/*Pg* amplitudes for the 1 to 4 Hz frequency band. This is the same model as that shown in Figure 10.

results are shown in Figure 15. These results reveal generally efficient *Sn* propagation in oceanic lithosphere and generally inefficient *Sn* propagation in the Anatolian and Iranian plateaus. However, in order to map the details of *Sn* propagation in the Middle East we have again used tomography. Unlike our study of *Lg*, because of the instability of the *Sn*/*Pn* ratios as well as the subtle nature of continental *Sn* in tectonically active regions, we chose to tomographically map qualitatively assigned *Sn* propagation efficiencies rather than amplitude ratios. This strategy allowed us to assign equal weights to the relatively weak *Sn* signals observed in the continents and the very strong *Sn* observed for oceanic paths because we are primarily interested in regions of *Sn* blockage and not the differences in *Sn* propagation in oceanic and continental lithosphere.

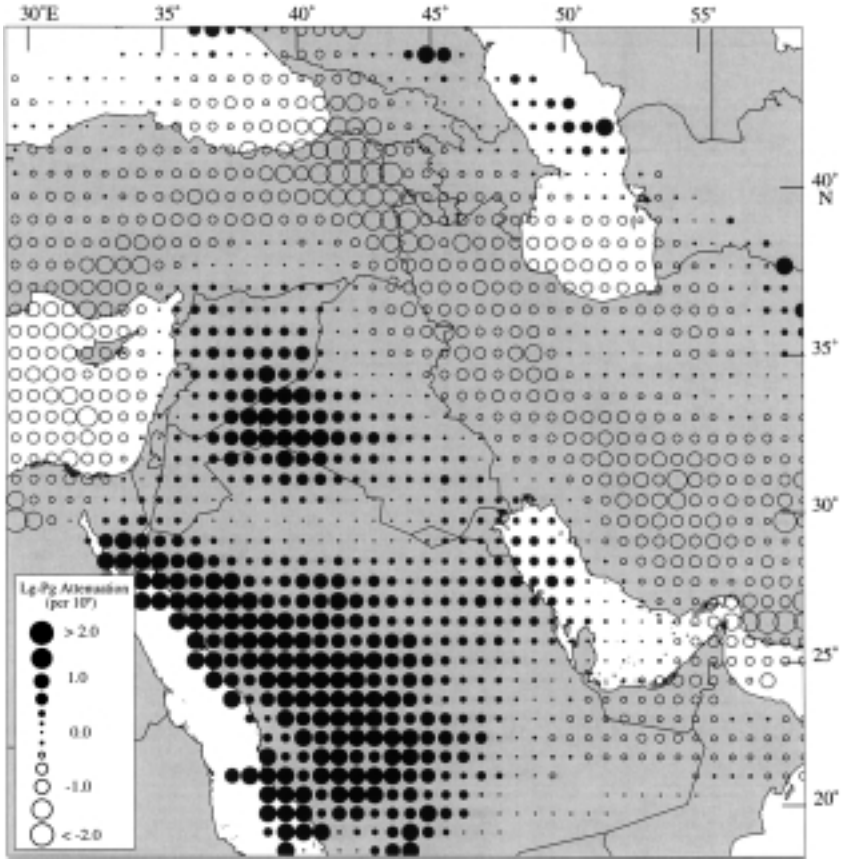

Figure 14b
A map showing a tomographic model of *Lg*/*Pg* amplitudes for the 0.5 to 2 Hz frequency band. This model is similar to the model shown in Figure 14a indicating the small amount of energy contained in the 2 to 4 Hz band. This also indicates that the short-period instrument responses have no significant effect on our *Lg*/*Pg* ratio calculations.

We assigned each seismogram to one of three categories: no *Sn*, efficient *Sn*, and weak or inefficient *Sn*. Although these categories are qualitative, we used strict criteria when evaluating each of the regional seismograms. If the seismogram showed no evidence of a discernable high-frequency *Sn* wavetrain, we categorized that path as ''no *Sn* present.'' If some *Sn* wavetrain could be observed, regardless of its strength or amplitude, we designated it ''efficient *Sn*.'' If there were some ambiguous signal in the seismogram that potentially could be an *Sn* signal, it was classified as ''weak or inefficient *Sn*.'' This category was seldom used since we could usually clearly delineate, with the use of bandpass filters and spectrogram analysis, between those seismograms with *Sn* and those which did not contain an *Sn* signal. We tended to use the ''inefficient *Sn*'' category for those seismograms at shorter distances where regional phases cannot always be easily identified, especially for continental paths.

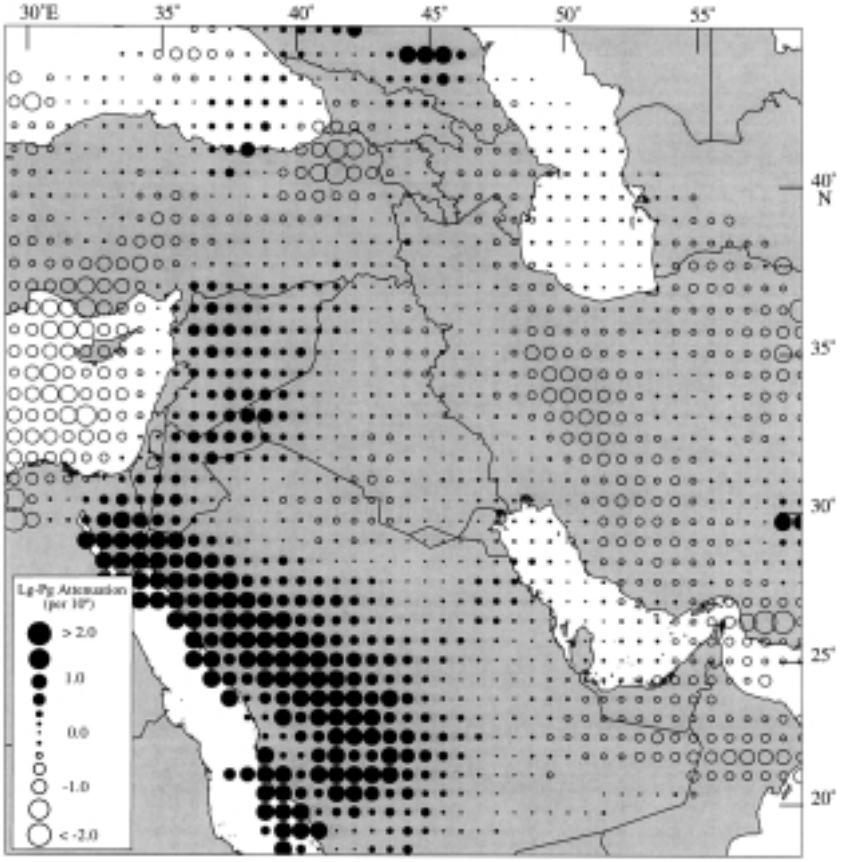

Figure 14c
A map showing a tomographic model of Lg/Pg amplitudes for the 2 to 4 Hz frequency band. This model is different than Figure 14a. We begin to see Lg attenuation in eastern Iraq and all along the deep sediments that correspond to the Mesopotamian foredeep.

Sn Efficiency Tomography Method

The method we used to tomographically image Sn propagation is similar to that used in our Lg/Pg study. However, we have chosen not to use amplitude ratios since we have found them to be primarily a function of whether the path was oceanic or continental. This is because continental Sn is generally a subtle phase which is not easily measured using amplitude ratios. Taking the logarithm of equation (2), neglecting the geometrical spreading term, discretizing the spatial attenuation factor, and substituting $\pi\, fm_l/V_{Sn}$ for α we obtain:

$$\log_{10}\left(\frac{a_{ij}^0}{a_{ij}}\right) = \log_{10} e \frac{\pi f}{V_{Sn}} \sum_l m_l l_{ijl} \tag{7}$$

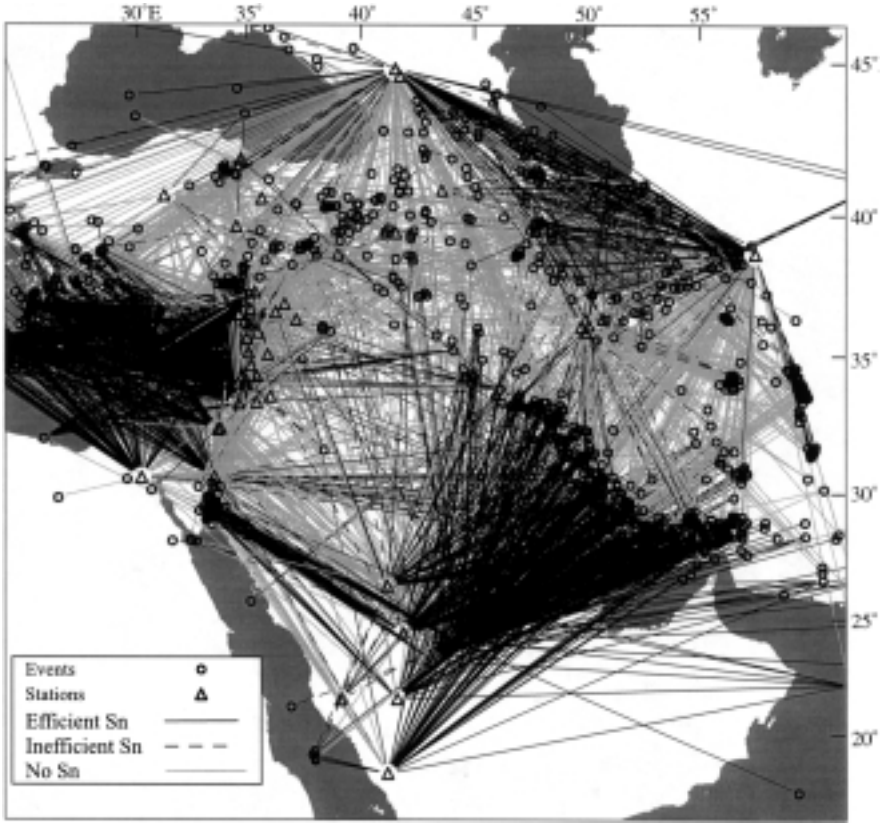

Figure 15
A map showing all 4200 *Sn* raypaths used in this study. The waveform for each raypath has been visually inspected using a variety of bandpass filters to identify if *Sn* is present or not. *Sn* attenuation for most continental paths in the northern Middle East is very clear.

where

$$a_{ij}^{0} = s_j(\omega)c_i(\omega)$$

where f is the frequency of the *Sn* signal (1 Hz), V_{Sn} is the velocity of *Sn* (4.6 km/s) and all variables and indices are the same as was used in equations (2) through (5). If we assume, to first order, that the effect of geometrical spreading will not play a major role in *Sn* blockage, we can discretize the data vector and use discrete wave propagation efficiencies rather than amplitudes or amplitude ratios.

$$\hat{A}_{ij}^{dsc} = \log_{10} e \frac{\pi f}{V_{Sn}} \sum_{l} m_l l_{jjl} \tag{8}$$

where

$$\hat{A}_{ij}^{dsc} = 1, 0.5, \quad \text{or} \quad 0.0 \ .$$

We assigned the propagation efficiencies as follows: 1 for no or blocked *Sn*, 0.5 for inefficient or weak *Sn*, and 0.0 for an efficient *Sn*. Equation (8) is very similar to the method of SAUNDERS *et al.* (1988), who used local analog seismograms to map regions of high attenuation. By choosing these three numbers for our propagation efficiencies we have defined both our model parameter as the reciprocal of the extinction path length and the necessary, albeit idealized, attenuation that defines blocked, inefficient and efficient *Sn*.
For

$$\hat{A}_{ij}^{dsc} = 1: \ a_{ij} = 0.1 \ a_{ij}^{0} \ (90\% \text{ attenuation})$$
$$\hat{A}_{ij}^{dsc} = 0.5: \ a_{ij} = 0.3 \ a_{ij}^{0} \ (70\% \text{ attenuation})$$
$$\hat{A}_{ij}^{dsc} = 0.0: \ a_{ij} = a_{ij}^{0} \ (0\% \text{ attenuation}) \ .$$

Using these definitions of efficient, inefficient and blocked *Sn*, our model parameters in equation (8), m_l, becomes the reciprocal of the extinction path length. Because we have created a set of idealized criteria defining our propagation efficiencies, it is important not to overinterpret our model parameters. In practice, because we have chosen to define efficient *Sn* as an indication of no attenuation at all, our results represent in effect the maximum extinction path length for *Sn*. We have allowed our model parameters to fall below zero if the data require it. We have interpreted the negative extinction path lengths as an indication that our assumption of no attenuation or very small attenuation for efficient *Sn* paths is incorrect for those regions. For the most part, only a few cells decreased significantly beneath zero.

Solving this linear set of equations (equation (8)) allows us to objectively and quantitatively map our qualitative *Sn* efficiencies (Fig. 16). We chose our Laplacian damping parameter using the same technique we used for our *Lg*/*Pg* tomography. In order to minimize the inversion artifacts for our *Sn* tomography we required larger weighting for the Laplacian damping. This is in part due to the discrete nature of our database as well as the longer path lengths that were required for our *Sn* observations although generally we had adequate ray coverage throughout most of our model (Fig. 17).

►

Figure 16
Maps showing the *Sn* efficiency tomographic model for all the rays shown in Figure 15. Blue indicates *Sn* spatial attenuation of 5×10^{-4} km^{-1} or lower (efficient *Sn*) while red indicates a spatial attenuation of 1.5×10^{-3} km^{-1} or greater (no *Sn*). White color corresponds to regions of inefficient *Sn* propagation or *Sn* attenuation that only occurs for path lengths of approximately 1000 km or greater. The thick green lines show the major tectonic boundaries in the Middle East.

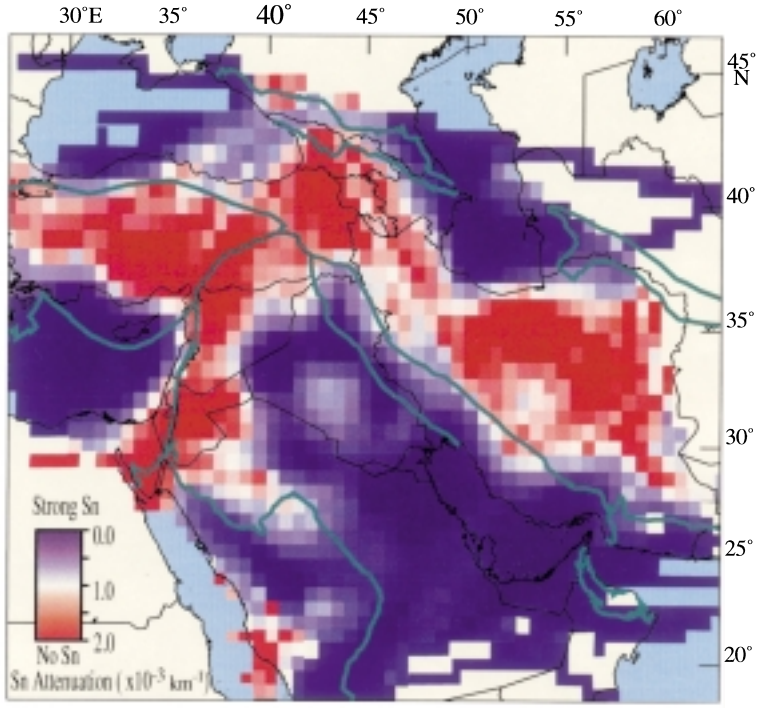
30°E
35°
40°
45°
50°
55°
60°
45° N
40°
35°
30°
25°
20°
Strong Sn
0.0
1.0
2.0
No Sn
Sn Attenuation (x10-3 km-1)

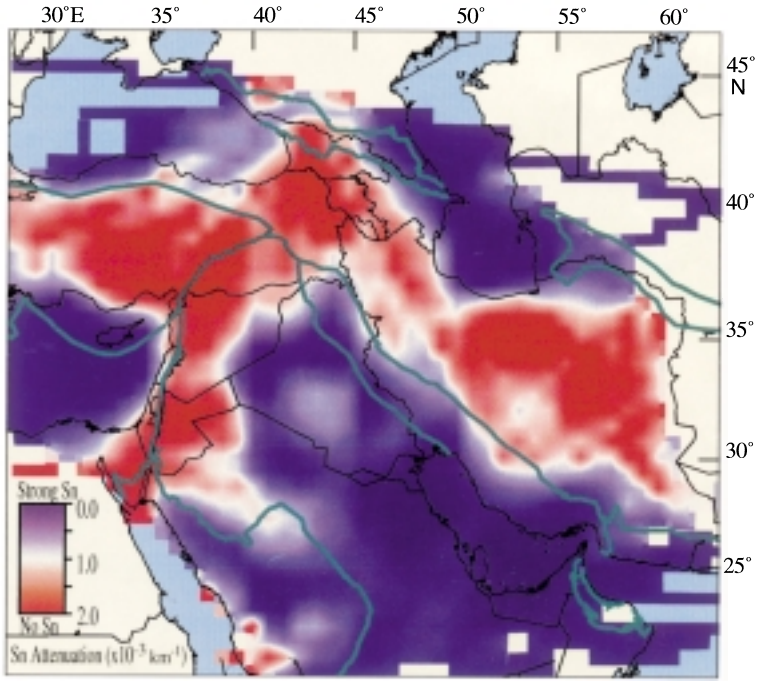
30°E
35°
40°
45°
50°
55°
60°
45° N
40°
35°
30°
25°
Strong Sn
0.0
1.0
2.0
No Sn
Sn Attenuation (x10-3 km-1)

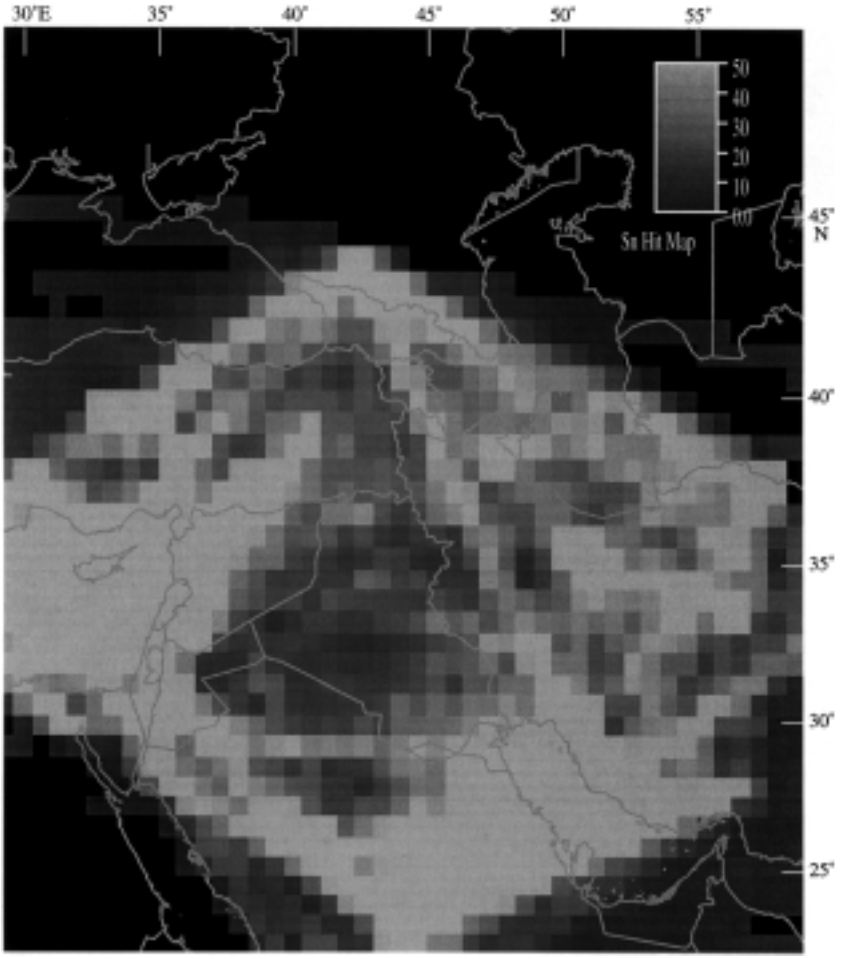

Figure 17
A map showing the hit count map for the tomographic model shown in Figure 16. Note the low number of hit counts in Iraq and some paths of northeastern Turkey.

Resolution and Uncertainties

In order to estimate the resolution of our *Sn* efficiency tomography we performed resolution tests as in our analysis of *Lg*/*Pg* ratio tomography. In order to reproduce a discrete synthetic data set we used a criterion to convert the non-discrete synthetic amplitude which is produced by propagating rays through a synthetic test model. We created a synthetic set of propagation efficiencies by defining an extinction path length. Assuming a minimum frequency for *Sn*, the extinction path length corresponds to a *Q* value:

$$Q = \frac{-\pi L^{\text{ext}} f}{V_{Sn} \ln(0.10)} \tag{10}$$

for example $V_{Sn} = 4.6$ km/s, $f = 1$ Hz, $L^{\text{ext}} = 250$ km, $Q = 75$ (Fig. 18). For the synthetic tests we did not create any inefficient *Sn* synthetic data, only efficient and blocked *Sn*, in order to make conservative estimates of our resolution. We also added ten percent noise by randomly switching 10% of our synthetic efficiencies from 1.0 to 0.0 or from 0.0 to 1.0. After creating a discrete synthetic set of *Sn* propagation efficiencies analogous to our actual data set, we used the Laplacian damped LSQR algorithm to solve for the input test model for a variety of extinction path lengths (Fig. 18). We used a variety of synthetic models to test our *Sn* model resolution including checkerboards, vertical strips, horizontal strips, and spike tests. Generally we observed the same resolution problems with all of the test models.

The apparent resolution is not as good as that of the *Lg*/*Pg* ratio tomography and depends upon our choice of the extinction path length. Our resolution tests

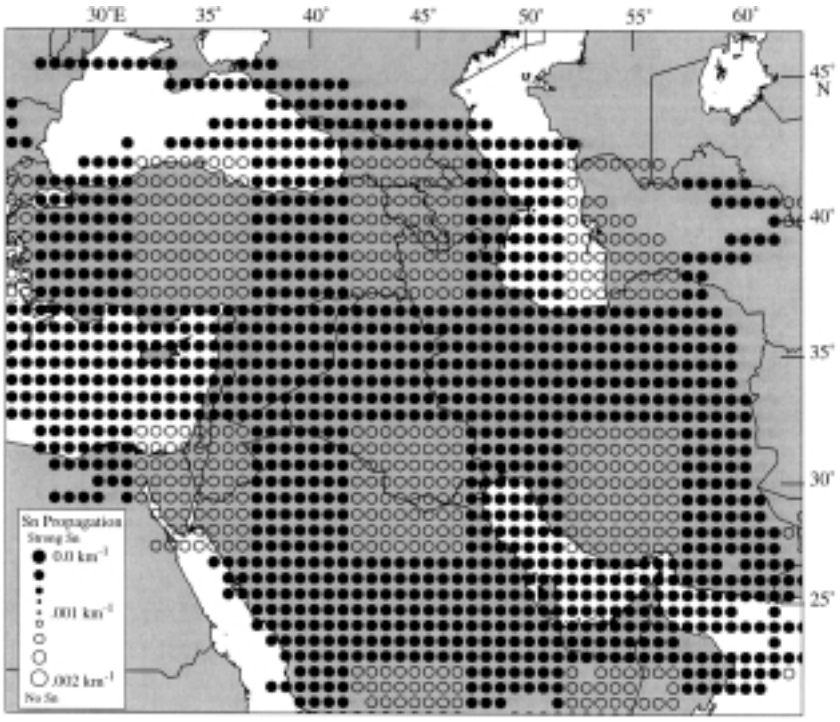

Figure 18a
A map showing the test model used to determine the resolution of our *Sn* efficiency tomography. This model contain "spikes" of regions with *Sn* extinction path lengths of 500 km surrounded by regions with no *Sn* attenuation (infinite extinction path length). Besides this test model we used a variety of other model geometries to test our model resolution.

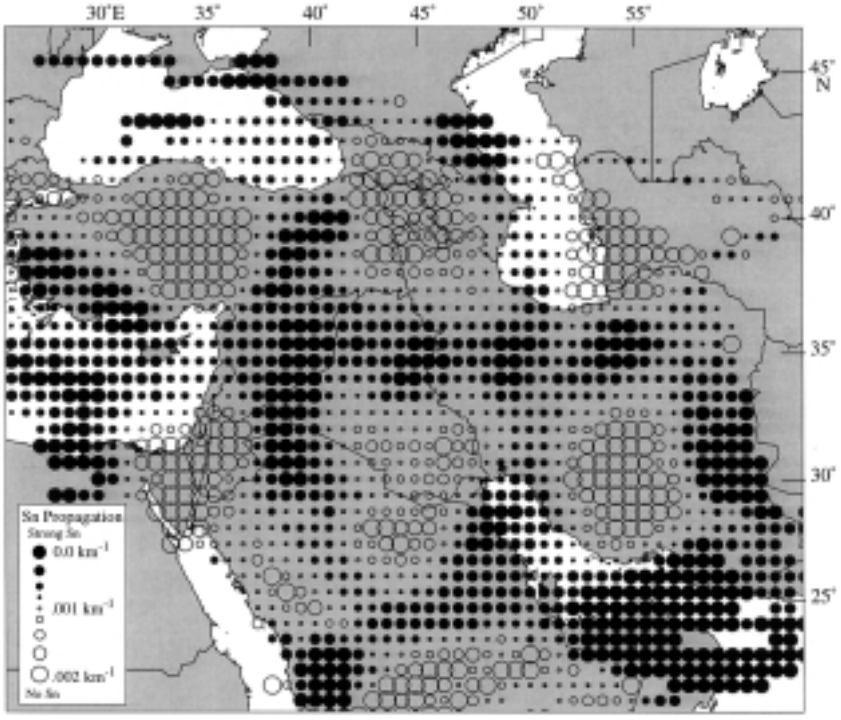

Figure 18b
A map showing the results of our resolution spike test using an extinction path length of 250 km in this test model. We observe east to west smearing of anomalies in northwestern Saudi Arabia as well as north-south smearing along the Red Sea and the Gulf of Aqaba.

demonstrate that conservatively only 200 to 300 km sized features, depending upon the degree of attenuation (i.e., extinction path length), can be resolved with our technique. This is not surprising given the large path length (greater than 300 km) that is required to observe *Sn*. We are able to image the original input model reasonably well in the eastern Mediterranean and Anatolian plateaus. However, in southern Arabia and Iran there is "smearing" in the east-west direction. This is mainly caused by the lack of stations and sources in central and southern Arabia. We also see north-south distortion of the test anomalies in the southern Zagros mountains. Examining Figure 18d we see that anomalies with extinction paths exceeding 500 km are not as well imaged as those anomalies with extinction paths of 250 km. In general, we cannot resolve attenuation anomalies where *Sn* is eliminated in 700 km or greater.

In order to estimate the uncertainties we employed the bootstrap resampling technique that we used for *Lg*/*Pg* tomography. By randomly resampling our original data set and reinverting for our model *Sn* propagation efficiencies 100 times, we were able to estimate the variance of each model parameter (Fig. 19).

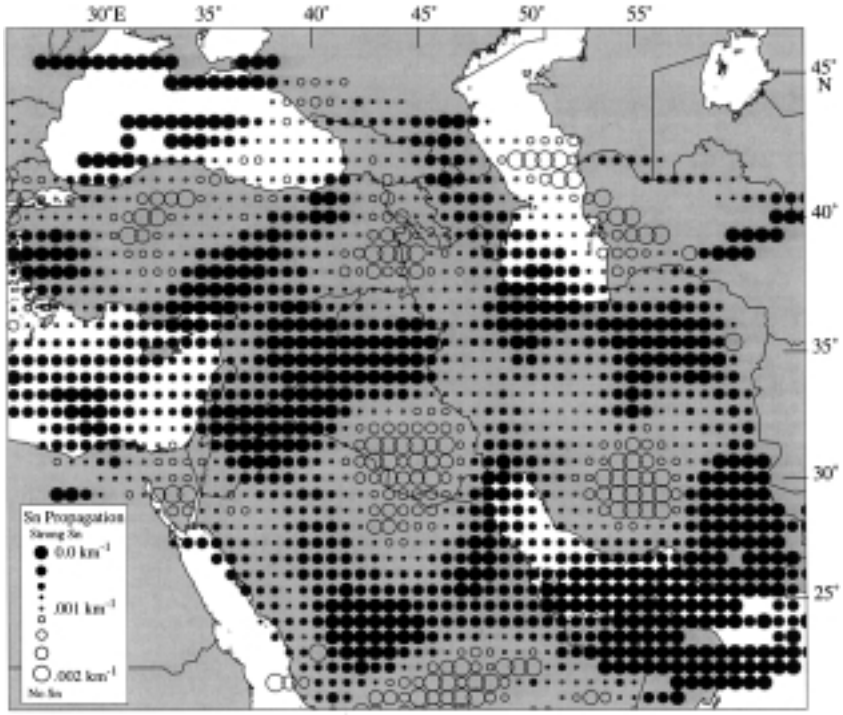

Figure 18c
A map showing the results of our resolution spike test using an extinction path length of 500 km. We still observe considerable amounts of smearing even with the less-attenuating test model.

We found that in general our estimated uncertainties were fairly minor. The exception is in Iraq and northern Saudi Arabia where we found substantial uncertainties in the model *Sn* efficiencies, indicating that these values are not very reliable. This is due, for the most part, to the lack of ray coverage in this part of our model (Fig. 17).

Results

The most obvious feature in our model is weak or no *Sn* propagation in Turkey and most of Iran, and efficient *Sn* propagation in the oceanic lithosphere as well as in most of the Arabian plate (Fig. 16). In both the Anatolian and the Iranian plateaus, *Sn* is heavily attenuated. The inefficient *Sn* zone in the Iranian plateau is bounded on the west by the Zagros fold and thrust belt and extends all the way to the East Iranian ranges (~60°E longitude) and as far south as the Makran in southern Iran. Throughout most of the Anatolian plateau and into the Anatolian block *Sn* propagation is inefficient. Similarly, in the Lesser Caucasus *Sn* is heavily attenuated; however, *Sn* propagation is efficient in the eastern half of the Greater Caucasus.

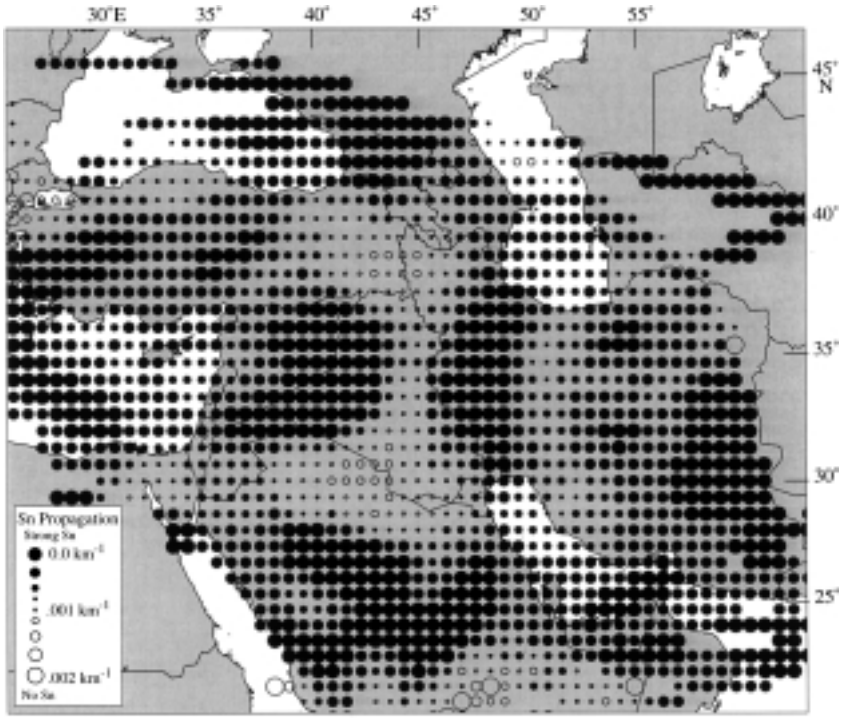

Figure 18d
A map showing the results of our resolution spike test using an extinction path length of 750 km. Note that we no longer can resolve the anomalies in central Turkey since the majority of our rays are not sufficiently long to be attenuated.

Our tomographic models indicate that the zone of inefficient *Sn* is not confined to the Anatolian plateau, but extends to the south across the Bitlis suture and into western Syria. Our resolution tests and uncertainty estimates indicate that this is neither an artifact nor a product of "smearing" of the inefficient *Sn* region within the Anatolian plateau. We also observe a large region of inefficient *Sn* that includes the southern Dead Sea fault in Jordan, Palestine, and Israel, as well as the Gulf of Aqaba. This region of *Sn* attenuation also extends approximately 500 km to the east, well into the northwestern segment of the Arabian plate. Some of this could be an artifact, as was demonstrated by our resolution tests in Figure 18. This feature could be due to smearing of the anomaly along the Dead Sea fault or perhaps the blurring together of two separate anomalies in the region; one in Jordan, Palestine, and Israel and the other in northern Saudi Arabia. Another region with similar resolution problems is the eastern Black Sea where we only have two stations in the Greater Caucasus recording a large number of events in the Anatolian plateau. This has caused the inefficient *Sn* zone in the Anatolian

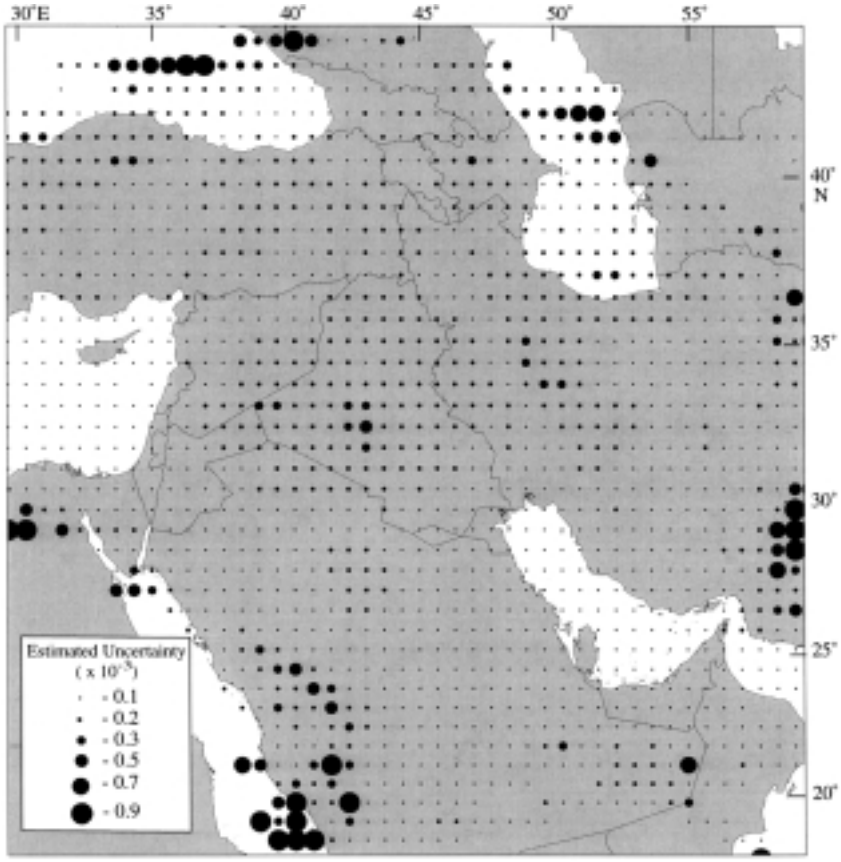

Figure 19
A map showing bootstrap uncertainty estimates for our *Sn* efficiency tomography. A bootstrap uncertainty of 0.5 corresponds to approximately 50% error for either most efficient *Sn* or blocked *Sn* anomalies shown in Figure 16. In general our tomographic model is fairly stable; however, in central Iraq and northern Saudi Arabia we have fairly large uncertainties approaching 50% of the anomalies shown in Figure 16.

plateau to "bleed" into the eastern Black Sea where we have scant model resolution.

Along the Red Sea coast in Saudi Arabia we observe another region of *Sn* attenuation which is based mostly on observations at two stations along the Red Sea coast (Figs. 4 and 16). To the northeast of this anomaly we found a region of efficient *Sn* propagation in the northern Arabian shield between the region of no *Sn* propagation along the Red Sea coast and inefficient *Sn* propagation in northern Saudi Arabia. Throughout most of southern and central Arabia, including Iraq and the Persian Gulf, *Sn* was found to be efficient. We have also found that *Sn* is efficient in the Koppeh Dagh region and farther to the west in the eastern Caucasus and in the Caspian Sea.

Discussion and Conclusions

The results of our *Lg*/*Pg* tomography are fairly consistent with prior studies of *Lg* in the Middle East. However, because of the considerably more waveform data used in this study we were able to accurately map the boundaries of *Lg* and *Sn* attenuation. The blockage of *Lg* phases across the Zagros mountains has been demonstrated by several different studies including KADINSKY-CADE *et al.* (1982), RODGERS *et al.* (1997), CONG and MITCHELL (1997), and MELLORS *et al.* (1999). In the Greater Caucasus, however, our results suggest a somewhat different picture from that suggested by KADINSKY-CADE *et al.* (1982) and RODGERS *et al.* (1997). We found that the region of complete *Lg* blockage resides in the easternmost edge of the Anatolian plateau in northeastern Turkey rather than in the Greater Caucasus, where for the most part we observe relatively efficient *Lg* propagation. Furthermore, we have found a very good correlation with inefficient *Lg* propagation and the Arabian plate boundary and the major tectonic provinces (Figs. 20 and 10). Prior studies (e.g., MITCHELL *et al.*, 1997; RODGERS *et al.*, 1997) found less of a correlation with *Lg* attenuation, probably because of the lack of resolution. Local network data from Syria and Turkey used in our study significantly improved our ability to resolve the geometry of *Lg* blockage and attenuation.

The boundaries marking regions of high *Lg* attenuation, relative to *Pg*, and regions of efficient *Lg* propagation correspond remarkably well with the boundary between the Eurasian and Arabian plates. This correlation is probably due to changes in crustal and sediment thickness across these boundaries. There is evidence for a crustal root beneath the Zagros mountain belt (e.g., SNYDER and BARAZANGI, 1986) as well as significantly thick sediments. This type of rapid crustal thickness variation has been demonstrated to block *Lg* (KENNETT, 1986). However, there is an approximately 100 to 200 km offset between the location of the crustal root and the location of minimum *Lg*-*Pg* differential attenuation. This might be due to the lack of seismic stations in the Iranian plateau which has led to most raypaths traveling from east to west in this region. This bias in our data set might cause smearing of the region of *Lg* blockage eastwards.

We observe similar types of *Lg* blockage in easternmost Anatolia. This may be a result of a sudden increased crustal thickness in eastern Turkey or perhaps to intrinsic attenuation in the crust caused by partial melt. We do not observe any *Lg* blockage for paths crossing the Dead Sea fault system. Any potential Moho topography and structural complexity associated with the Dead Sea fault are ▶

Figure 20

Maps showing several independent data sets which may be correlated with both our *Lg*/*Pg* and *Sn* efficiency tomography results. Panel (a) shows both the topography of the Middle East as well as Holocene volcanoes and Neogene volcanic fields. Panel (b) shows the *Pn* velocity map of HEARN and NI (1994). Regions of high topography generally have high *Lg* attenuation relative to *Pg*. We also see a fairly good correlation between low *Pn* velocities shown in panel (b) and high *Sn* attenuation.

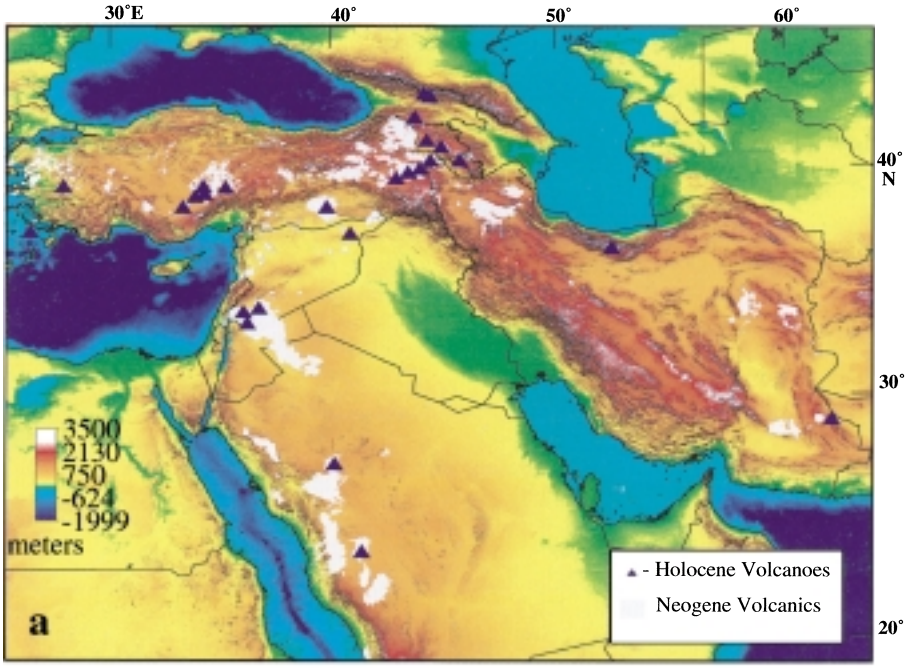
30°E
40°
50°
60°
40° N
30°
20°
3500
2130
750
-624
-1999
meters
▲ - Holocene Volcanoes
Neogene Volcanics
a

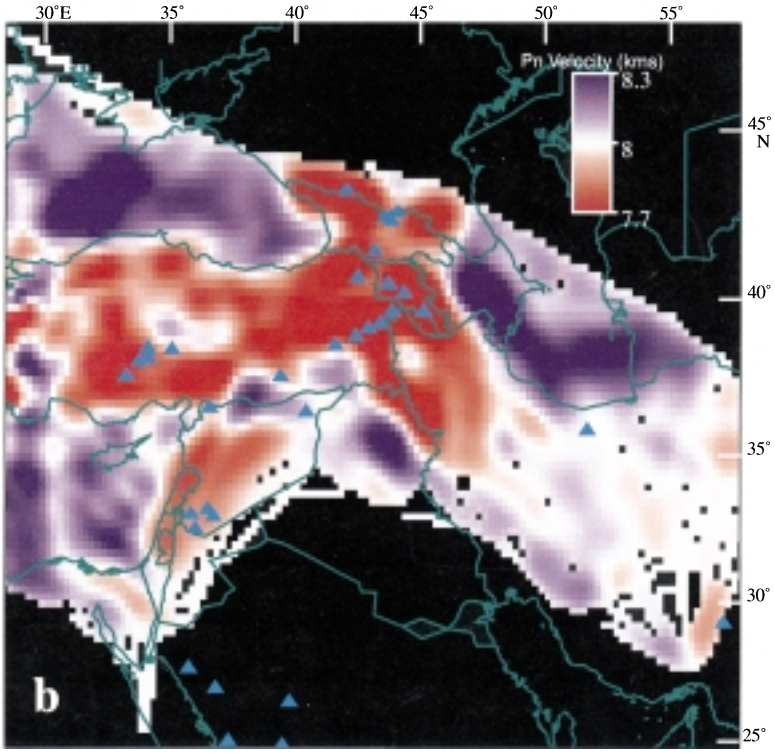
30°E
35°
40°
45°
50°
55°
Pn Velocity (kms)
8.3
8
7.7
45° N
40°
35°
30°
25°
b

apparently insufficient to disrupt *Lg* propagation, unlike the other major plate boundaries in the Middle East. The importance of sediment thickness on *Lg* propagation can be seen from the patterns of observed *Lg*/*Pg* amplitude ratio variation in Saudi Arabia. In the west, where no sedimentary rocks are present, *Lg* clearly propagates more efficiently than in the Arabian platform where sediment thickness ranges between 5 and 15 km (HUSSEINI, 1988). There is a region of similarly efficient *Lg* propagation in central and western Iraq which correlates with the Rutbah uplift as mapped by LOVELOCK (1984) and BREW *et al.* (1997).

We observe a small region in central Iran where *Lg* propagation is somewhat efficient, especially for lower frequencies, contrasting with the complete *Lg* blockage we observe across the Zagros fold and thrust belt. There is very little known about the crustal structure of this region. Raypaths associated with efficient *Lg* propagation in central Iran are shown in Figure 8. These observations suggest that the crustal structure in central Iran is less variable than other parts of the Iranian plateau where we do not observe as efficient *Lg* propagation. In the Makran region of southern Iran, however, we see very large regions of complete *Lg* blockage which again could be produced by a combination of crustal thickness variations in Oman and the Makran along with the oceanic crust in the Gulf of Oman (RAVAUT, *et al.* 1997). However, there is a large amount of Holocene volcanism in the Makran which could be indicative of partial melt in the crust which also would block *Lg*. North of Iran, in the Caspian Sea, there is a clear boundary between what appears to be remnant oceanic crust in the south Caspian (ZONENSHAIN and LEPICHON, 1986) and what appears to be thicker crust in the north Caspian Sea.

When interpreting uppermost mantle structure using wave propagation, efficient *Sn* typically implies a relatively cold/thick mantle lithosphere, such as most old oceanic lithosphere, where uppermost mantle attenuation is small. Poor *Sn* propagation, which is indicative of high uppermost mantle attenuation, implies hotter uppermost mantle and perhaps the presence of partial melt. However, it is not necessary to have partial melt in the uppermost mantle to substantially (5 to 10 times) lower *Q* (KAMPFMANN and BERCKHEMER, 1985; SATO *et al.*, 1989); therefore inefficient *Sn* propagation could also be an indication of simply hot lithosphere as opposed to a region of asthenospheric upwelling. Attempts at modeling *Sn* wavetrains have indicated that a negative velocity gradient is required in the uppermost mantle (lithosphere-asthenosphere boundary) in order to produce an effective waveguide for *Sn* (STEPHENS and ISACKS, 1977). If this velocity gradient were reduced or altered, then *Sn* propagation could conceivably be attenuated or perhaps in some cases blocked.

To first order, our tomographically mapped regions of poor *Sn* propagation in the Middle East agree with the prior work of KADINSKY-CADE *et al.* (1982), RODGERS *et al.* (1997), and MELLORS *et al.* (1999). However, there are important differences to note. In general, we map larger regions of poor *Sn* propagation than KADINSKY-CADE *et al.* (1982) and RODGERS *et al.* (1997). This is especially evident

when examining the region of inefficient *Sn* in Iran, where we found that *Sn* does not propagate across the entire Iranian plateau. Similarly *Sn* does not propagate within the Anatolian plateau. Furthermore, we found a very large region of poor *Sn* propagation along the southern Dead Sea region that extends into eastern Jordan. A portion of this inefficient *Sn* zone could be due to resolution problems in our tomographic model. However, given the extensive *Sn* attenuation that we observe at stations in Saudi Arabia, Egypt, and southern Israel, this zone of uppermost mantle attenuation must be fairly substantial. We would suggest that most of western Jordan and western Syria is underlain by this zone of uppermost mantle attenuation. The region of *Sn* attenuation along the Red Sea coast agrees well with the study of MELLORS *et al*. (1999), with the exception that along the northeastern Red Sea coast we have observed efficient *Sn* propagation that extends in the Arabian shield for approximately 500 km.

Comparison of our *Sn* attenuation with the *Pn* velocity tomography of HEARN and NI (1994) can eliminate some of the ambiguity in interpreting individual observations. Generally there is a fairly good correlation between lower *Pn* velocities (7.6–7.8 km/s) and our regions of *Sn* attenuation, with a few notable exceptions (Fig. 20). For the most part central and eastern Turkey as well as the Lesser Caucasus have generally low *Pn* velocity (~7.75 km/s) and inefficient *Sn* propagation. These observations are an indication that there is partial melt in the uppermost mantle beneath the Anatolian plateau and the northwestern corner of the Iranian plateau. This observation is confirmed, to some degree, by the large amount of Quaternary and active volcanism in the Plateau (Fig. 20). However, we also find very important differences between the two tomographic models. The most striking difference is the region of high *Pn* velocity (8.2 km/s) south of the Bitlis suture in southeastern Turkey where we also see inefficient *Sn* propagation. Although this could be due to a lack of resolution by both tomographic models, this is the region with the best ray coverage for our *Sn* attenuation tomography. This observation is also interesting since there is evidence of Quaternary volcanism south of the Bitlis suture. Perhaps it is an indication of strong lateral heterogeneity or azimuthal seismic anisotropy affecting the *Pn* velocity measurements.

Another important result of our study is the large area of *Sn* attenuation in the Iranian plateau, especially since the study of HEARN and NI (1994) did not find particularly low *Pn* velocities (7.9–8.1 km/s). Again, this might be the bias towards *Sn* blockage in the Iranian plateau caused by the predominantly long raypaths in this region. Similarly this observation might indicate a lack of partial melt in the lithospheric mantle although perhaps the lithosphere is still hot and not fully recovered from the substantial volcanism in the late Cenozoic. This hypothesis is also consistent with the lack of extensive Holocene volcanism within the Iranian plateau (Fig. 20).

One of the most interesting regions of *Sn* attenuation in the Middle East occurs in Israel, Palestine, and most of Jordan. It is possible that this anomaly is artificially

enlarged due to the lack of stations and sources in this region. However, complete elimination of *Sn* waves traveling from the Eastern Mediterranean Sea into Saudi Arabia (see Figs. 4 and 15) suggests that this zone is substantial (i.e., 200–400 km). There is little evidence for lower uppermost mantle velocities in the Gulf of Aqaba (HOFSTETTER *et al.*, 1991) and the Dead Sea fault system (GINZBURG and MAKRIS, 1979). However, few measurements of uppermost mantle velocity have been made farther east in Jordan and Saudi Arabia. Based on the Quaternary volcanism in this region (Fig. 20), CAMP and ROOBOL (1992) have proposed a broad zone of upwelling asthenosphere in western Arabia. Our observations suggest that the lithosphere is not hot or thinned across the entire Arabian shield.

Results from regional wave propagation tomography offer new and important insight into the attenuation structure of the crust and uppermost mantle. However, further resolution and reliable criteria must be developed to eliminate some of the ambiguity in the interpretation of the behavior of regional waveforms. However, in order to unambiguously determine the path effects on *Lg* propagation we need to better account for source contributions to *Lg* excitation. Even though we have not fully accounted for the source effects, given our data redundancy our *Lg-Pg* differential attenuation model can be used to correct *Lg*/*Pg* ratios for the path effects, which is critical to reliably discriminating earthquakes from explosions in the Middle East, given the dramatic variations in *Lg* and *Pg* propagation.

Acknowledgments

We thank the Syrian National Seismological Center of the General Establishment of Geology and Mineral Resources (Damascus, Syria) and the Kandilli Observatory and Earthquake Research Institute of Bogaziçi University (Istanbul, Turkey) for providing us data for this study and for the maintenance of their networks. We would like to thank Scott Phillips for providing special insight into our *Lg-Pg* tomographic method. We also are grateful to Christine Orgren and Francisco Gomez for their useful comments and discussions. We would especially like to thank Brian Mitchell for his reivew of our manuscript. The Cornell researchers are supported by a grant from the Defense Threat Reduction Agency of the Department of Defense No. DSWA01-97-1-0006. INSTOC contribution No. 257.

REFERENCES

BARKA, A., and REILINGER, R. (1997), *Active Tectonics of the Eastern Mediterreanean Region: Deduced from GPS, Neotectonic and Seismicity Data*, Annali Di Geofisica *40*, 587–610.

BAUMGARDT, D. R. (1996), *Investigations of Lg Blockage and Transportability of Regional Discriminants in the Middle East*, Sci. Report 1, PL-TR-96-2294, ENSCO Inc., Springfield, Virginia.

BAUMGARDT, D. R., and DER, Z. (1997), *Investigation of the Transportability of the P/S Ratio Discriminat to Different Tectonic Regions*, Sci. Report 1, PLT-TR-94-229, ENSCO, Inc., Springfield, Virginia.

BERBERIAN, M., and KING, G. (1981), *Towards a Paleogeography and Tectonic Evolution of Iran*, Can. J. Earth Sci. *18*, 33–69.

BOSTOCK, M., and KENNETT, B. L. N. (1990), *The Effect of 3-D structure on Lg Propagation Patterns*, Geophys. J. Int. *101*, 355–365.

BOUCHON, M. (1982), *Complete Synthesis of Seismic Crustal Phases at Regional Distances*, J. Geophys. Res. *87*, 1,735–1,741.

BREW, G., LITAK, R., SEBER, D., BARAZANGI, M., AL-IMAM, A., and SAWAF, T. (1997), *Basement Depth and Sedimentary Velocity Structure in the Northern Arabian Platform, Eastern Syria*, Geophys. J. Int. *128*, 617–631.

CAMP, V. C., HOOPER, P. R., ROOBOL, M. J., and WHITE, D. L. (1987), *The Madinah Eruption, Saudi Arabia: Magma Mixing and Simultaneous Extrusion of Three Basaltic Chemical Types*, Bull. Volcanol. *49*, 489–508.

CAMP, V. E., and ROOBOL, M. J. (1992), *Upwelling Asthenosphere Beneath Western Arabia and its Regional Implications*, J. Geophys. Res. *97*, 15,255–15,271.

CONG, L. L., XIE, J. K., and MITCHELL, B. (1996), *Excitation and Propagation of Lg from Earthquakes in Central Asia with Implications for Explosion/Earthquake Discrimination*, J. Geophys. Res. *101*, 27,779–27,789.

CONG, L., and MITCHELL, B. (1998), *Lg Coda Q and its Relation to the Geology and Tectonics of the Middle East*, Pure appl. geophys. *153*, 563–585.

DERCOURT, J., ZONENSHAIN, L., RICOU, L., KAZMIN, V., LE PICHON, X., KNIPPER, A., GRANDJACQUET, C., SBORTSHIKOV, I., GEYSSANT, J., LEPVRIER, C., PECHERSKY, D., BOULIN, J., SIBUET, J., SAVOSTIN, L., SOROKHTIN, O., WESTPHAL, M., BAZHENOV, M., LAUER, J., and BIJU-DUVAL, B. (1986), *Geological Evolution of the Tethys Belt from the Atlantic to the Pamirs since the Liasic*, Tectonophysics *123*, 241–315.

DEWEY, J. F., HEMPTON, M. R., KIDD, W. S. F., and SENGOR, A.M.C., *Shortening of Continental Lithosphere: The Neotectonics of Eastern Anatolia, a Young Collision Zone* (eds. Coward, M. P. *et al.*, 1986) Geological Society Special Publications *19*, 3–36.

DOTDUYEV, S., I. (1986), *Nappe Structure of the Greater Caucasus Range*, Geotectonics *20*, 420–430.

FAN, G., and LAY, T. (1998), *Statistical Analysis of Irregular Wave Guide Influences on Regional Seismic Discriminants in China*, Bull. Seismol. Soc. Am. *88*, 74–88.

FREUND, R. (1970), *The Geometry of Faulting in Galilee*, Isr. J. Earth Sci. *19*, 200–227.

GARFUNKEL, Z. (1981), *Internal Structure of the Dead Sea Leaky Transform (Rift) in Relation to Plate Kinematics*, Tectonophysics *80*, 81–108.

GINZBURG, A., and MAKRIS, J. (1979), *Gravity and Density Distribution in the Dead Sea Rift and Adjoining Areas*, Tectonophysics *54*, 17–25.

GHALIB, H. A. A. (1992), *Seismic Velocity Structure and Attenuation of the Arabian Plate*, Ph.D. Dissertation, Saint Louis University, pp. 260–288.

GREENWOOD, W. R., ANDERSON, R. E., FLECK, R. J., and ROBERTS, R. J., (1980), *Precambrian Geologic History and Plate Tectonic Evolution of the Arabian shield*. Saudi Arabian Directorate for Miner. Resources Bull., pp. 24–35.

HARTSE, H., FLORES, R., and JOHNSON, P. (1998), *Correcting Regional Seismic Discriminants for Path Effects in Western China*, Bull. Seismol. Soc. Am. *88*, 596–608.

HEARN, T., and NI, J. (1994), *Pn Velocities Beneath Continental Collision Zones: The Turkish-Iranian Plateau*, Geophys. Int. *117*, 273–283.

HOFSTETTER, A., FELDMAN, L., and ROTSTEIN, Y. (1991), *Crustal Structure of Israel: Contraints from Teleseismic and Gravity Data*, Geophys. J. Int. *104*, 371–379.

HUESTIS, S., MOLNAR, P., and OLIVER, J. (1973), *Regional Sn Velocites and Shear Velocity in the Uppermost Mantle*, Bull. Seismol. Soc. Am. *63*, 469.

HUSSEINI, M. (1988), *The Arabian Infracambrian Extensional System*, Tectonophysics *148*, 93–103.

JACKSON, J. A., and MCKENZIE, D. (1988), *The Relationship Between Plate Motions and Seismic Moment Tensors, and the Rates of Active Deformation in the Mediterranean and Middle East*, Geophys. J. *93*, 45–73.

KADINSKY-CADE, K., BARAZANGI, M., OLIVER, J., and ISACKS, B. (1981), *Lateral Variations in High Frequency Seismic Wave Propagation at Regional Distances across the Turkish and Iranian Plateaus*, J. Geophys. Res. *86*, 9,377–9,396.

KADINSKY-CADE, K., and BARAZANGI, M. (1982), *Seismotectonics of Southern Iran: The Oman Line*, Tectonics *1*, 389–412.

KAMPFMANN, W., and BERCKHEMER, H. (1985), *High Temperature Experiments on the Elastic and Anelastic Behavior of Magmatic Rocks*, Phys. Earth Planet. Int. *40*, 223–247.

KENNETT, B. L. N. (1986), *Lg Waves and Structural Boundaries*, Bull. Seismol. Soc. Am. *76*, 1,133–1,141.

LOVELOCK, P. E. R. (1984), *A Review of the Tectonics of the Northern Middle East Region*, Geol. Mag. *121*, 577–587.

INNOCENTI, F., MAZZUOLI, R., PASQUARE, G., RADICATI DI BROZOLO, F., and VILLARI, L. (1982), *Tertiary and Quaternary Volcanism of the Erzurum-Kars Area (Eastern Turkey): Geochronological Data and Geodynamic Evolution*, J. Volcanol. Geotherm. Res. *13*, 223–240.

MANGINO, S., and PRIESTLEY, K. (1998), *Crustal Structure in the Caspian Sea Region*, Geophys. J. Int. *133*, 630–648.

MCNAMARA, D., Owens, T., and WALTER, W. (1995), *Observations of Regional Phase Propagation Across the Tibetan Plateau*, J. Geophys. Res. *100*, 22,215–22,229.

MCKENZIE, D. (1972), *Active Tectonics of the Mediterreanean*, Geophys. J. R. Astr. Soc. *30* (2), 109–185.

MCKENZIE, D. (1976), *The East Anatolian Fault: A Major Structural in Eastern Turkey*, Earth Planet. Sci. Lett. *29*, 189–193.

MELLORS, R., VERNON, F., CAMP, V., AL-AMRI, A., GHALIB, A., and AL-DAIL, M. (1999), *Regional Waveform Propagation in the Saudi Arabian Peninusla*, Geophys. Res. Lett., in press.

MEYERS, S., BECK, S., ZANDT, G., and WALLACE, T. (1998), *Lithospheric-scale Structure across the Bolivian Andes from Tomographic Images of Velocity and Attenuation for P and S Waves*, J. Geophys. Res. *103*, 21,233–21,252.

MITCHELL, B. J., PAN, Y., XIE, J., and CONG, L. (1997), *Lg coda Q Variation across Eurasia and its Relation to Crustal Evolution*, J. Geophys. Res. *102*, 22,767–22,779.

MOLNAR, P., and OLIVER, J. (1969), *Lateral Variations of Attenuation in the Uppermost Mantle and Discontinuities in the Lithosphere*, J. Geophys. Res. *74*, 2,648–2,683.

NI, J., and BARAZANGI, M. (1983), *High Frequency Seismic Wave Propagation Beneath the Indian Shield, Himalayan Arc, Tibetan Plateau and the Surrounding Regions: High Uppermost Mantle Velocities and Efficient Sn Propagation Beneath Tibet*, Geophys. J. R. Astr. Soc. *72*, 665–689.

NOLET, G., *Seismic wave propagation and seismic tomography*. In *Seismic Tomography* (ed. NOLET, G., 1988), pp. 1–23.

NUTTLI, O. (1980), *The Excitation and Attenuation of Seismic Crustal Phases in Iran*, Bull. Seismol. Soc. Am. *70*, 469–480.

PAIGE, C. C., and SAUNDERS, M. A. (1982), *LSQR: An Algorithm for Sparse Linear Equations and Sparse Least Squares*, ACM Trans. Math. Software *8*, 43–71.

PEARCE, J. A., BENDER, J. F., DE LONG, S. E., KIDD, W. S. F., LOW, P. J., GUNER, Y., SAROGLU, F., YILMAZ, Y., MOORBATH, S., and MITCHELL, J. G. (1990), *Genesis of Collision Volcanism in Eastern Anatolia, Turkey*, J. of Volc. and Geotherm. Res. *44*, 189–229.

PHILLIP, H., CISTERNAS, A., GVISHIANI, A., and GORSHKOV, A. (1989), *The Caucnasus: An Actual Example of the Initial Stages of Continental Collision*, Tectonophysics *161*, 393–398.

PHILLIPS, W. S., HARTSE, H. E., TAYLOR, S., VELASCO, A. A., and RANDALL, G. E. (1999), *Regional Phase Amplitude Ratio Tomography for Seismic Verification*, submitted to Pure appl. geophys.

POWERS, R. W., RAMIREZ, L. F., REDMOND, C. P., and ELBERG, E. L. (1966), *Geology of the Arabian Peninsula: Sedimentary Geology of Saudi Arabia*, U.S. Geol. Surv. Prof. Pap., 560–D, 91–96.

PRESS, F., and EWING, M. (1952), *Two Slow Surface Waves across North America*, Bull. Seismol. Soc. Am. *42*, 219–228.

QUENNELL, A. M. (1959), *Tectonics of the Dead Sea Rift*, Int. Geol. Congr., 20th, Mexico, 1956 –Assoc. Sewrv. Geol Afr., 385–405.

RAVAUT, P., BAYER, R., HASSANI, R., ROUSSET, D., and AL YAHYA'EY, A. (1997), *Strcuture and Evolution of the Northern Oman Margin: Gravity and Seismic Constraints over the Zagros-Makran-Oman Collision Zone*, Tectonophysics *279*, 253–280.

REILINGER, R., MCCLUSKY, S., ORAL., B., KING, R., TOKSÖZ, N., BARKA, A., KINIK, I., LENK, O., and SANLI, I. (1997), *Global Positioning System Measurements of Present-day Crustal Movements in the Arabia-Africa-Eurasia Plate Collision Zone*, J. Geophys. Res. *102*, 9,983–9,999.

RODGERS, A., NI, J., and HEARN, T. (1997), *Propagation Characteristics of Short-period Sn and Lg in the Middle East*, Bull. Seismol. Soc. Am. *87*, 396–413.

SATO, H., SACKS, S., MURASE, T., MUNCIL, G., and FUKUYAMA, H. (1989), *Qp Melting Temperature Relation in Peridotite at High Pressure and Temperature: Attenuation Mechanism and Implications for the Mechanical Properties of the Uppermost Mantle*, J. Geophys. Res. *94*, 10,647–10,661.

SEARLE, R. C. (1975), *The Dispersion of Surface Waves across the Afar*. In *Afar Depression of Ethiopa* (eds. A. Pilgerand and A. Roesler) (Schweizerbart, Stuttgart, Germany) pp. 113–120.

SEBER, D., and MITCHELL, B. (1992), *Attenuation of Surface Waves across the Arabian Peninsula*, Tectonophysics *204*, 137–150.

SEBER, D., VALLVE, M., SANDVOL, E., STEER, D., and BARAZANGI, M. (1997), *Middle East Tectonics: Applications of Geographic Information Systems (GIS)*, GSA Today *7*, 1–6.

SENGOR, A. M. C., and KIDD, W. S. F. (1979), *Post-collisional Tectonics of the Turkish-Iranian Plateau and a Comparison with Tibet*, Tectonophysics *55*, 361–376.

SNYDER, D., and BARAZANGI, M. (1986), *Deep Crustal Structure and Flexure of the Arabian Plate Beneath the Zagros Collisional Mountain Belt as Inferred from Gravity Observations*, Tectonics *5*, 361–373.

STEPHENS, C., and ISACKS, B. (1977), *Toward an Understanding of Sn: Normal Modes Love Waves in an Oceanic Structure*, Bull. Seismol. Soc. Am. *67*, 69–78.

WIER, S. (1982), *Inefficient Propagation of Sn Under Southeastern China*, Geophys. J. R. Astr. Soc. *71*, 151–158.

ZHANG, T. R., and LAY, T. (1995), *Why the Lg Phase Does not Traverse Oceanic Crust*, Bull. Seismol. Soc. Am. *85*, 1665–1678.

ZONENSHAIN, L., and LEPICHON, X. (1986), *Deep Basins of the Black Sea and Caspian Sea as Remanants of Mesozoic Back-Arc Basins*, Tectonophysics, *123*, 181–211.

(Received July 14, 1999, revised January 19, 2000, accepted February 1, 2000)